Optical Engineering

SPIEDigitalLibrary.org/oe

Generalized camera calibration model for trapezoidal patterns on the road

Clement Chun Cheong Pang
Seakay Siqi Xie
Sze Chun Wong
Keechoo Choi

Optical Engineering 52(1), 017006 (January 2013)

Generalized camera calibration model for trapezoidal patterns on the road

Clement Chun Cheong Pang
Seakay Siqi Xie
Sze Chun Wong
The University of Hong Kong
Institute of Transport Studies
Department of Civil Engineering
Pokfulam Road
Pokfulam, Hong Kong
E-mail: cccpang@hku.hk

Keechoo Choi
Ajou University
TOD-Based Sustainable Urban Transportation Center, Department of Transportation Engineering
San 5, Woncheon-dong, Yeongtong-gu
Suwon 443-749, Korea

Abstract. We introduce a generalized camera calibration model that is able to determine the camera parameters without requiring perfect rectangular road-lane markings, thus overcoming the limitations of state-of-the-art calibration models. The advantage of the new model is that it can cope in situations where road-lane markings do not form a perfect rectangle, making calibration by trapezoidal patterns or parallelograms possible. The model requires only four reference points—the lane width and the length of the left and right lane markings—to determine the camera parameters. Through real-world surveying experiments, the new model is shown to be effective in defining the 2D/3D transformation (or vice versa) when there is no rectangular pattern on the road, and can also cope with trapezoidal patterns, near-parallelograms, and imperfect rectangles. This development greatly increases the flexibility and generality of traditional camera calibration models. [DOI: 10.1117/1.OE.52.1.017006]

Subject terms: Camera calibration; camera model; camera parameters; road-lane markings; perspective transformation; surveying; image metrology; visual traffic surveillance.

Paper 121406 received Sep. 26, 2012; revised manuscript received Nov. 30, 2012; accepted for publication Dec. 4, 2012; published online Jan. 30, 2013.

1 Introduction

The main purpose of camera calibration is to compute the camera parameters that define the relationship between two-dimensional (2-D) image coordinates and three-dimensional (3-D) world coordinates, which is essential for determining the dimensions and speeds of vehicles in visual traffic surveillance (VTS).[1,2] The role of camera recalibration is even more important in the case of surveillance cameras, which commonly contain pan-tilt-swing (PTZ) functions.[3,4] Producing man-made markers, such as erecting two posts on the roadside or marking a specific pattern on the road, is generally ineffective and impractical for calibration.[5,6] It is preferable to use existing patterns, such as road-lane markings, that can readily be found on the road as the reference points for calibration.[7]

State-of-the-art camera calibration models such as those proposed by Fung et al.[8] and He and Yung[9] rely on perfect rectangles defined by the four endpoints of road-lane markings [Fig. 1(a)]. In reality, lane markings do not always form perfect rectangles, especially when they are misaligned in the direction of the road, causing serious errors in calibration [Fig. 1(b)].[4] In some cases, such as in crosswalk areas where there are no road-lane markings, alternative markers such as crosswalk markings or box-markings need to be used for calibration, although they seldom form perfect rectangles (Fig. 2). The models of Fung et al.[8] and He and Yung[9] are not applicable in such circumstances.

To overcome this limitation, the models in Refs. 8 and 9 need to be generalized so that the camera parameters can be determined even when the existing rectangular pattern is imperfect or there is no rectangular pattern at all. This would make camera calibration possible under these challenging but inevitable situations. It is the aim of this paper to propose and test such a generalized calibration model.

The remainder of this paper is organized as follows. The problem analysis and literature review are presented in Secs. 2 and 3. The mathematical details of the proposed generalized camera calibration model are discussed in Sec. 4. The experimental results are presented and discussed in Sec. 5, and the conclusions are drawn in Sec. 6.

2 Problem Analysis

Geometrically, a perfect rectangle defined by lane markings has two degrees of freedom: the length (L) and width (W) [Fig. 3(a)]. However, in reality, lane markings may not be perfectly aligned [Fig. 3(b)]. In this case, if it is considered as a perfect rectangle, then the actual width W' will be misinterpreted as W, thus introducing an error, ε, which is the offset between the two lane markings. It can be observed from Fig. 3(b) that W' will increase as ε increases, thus $|W' - W|$ will also increase, resulting in even greater misinterpretation. In such cases, the models in Refs. 8 and 9 produce unacceptable errors. The situation is even worse when the offset between points A and C is not equal to that between points B and D.

With this observation in mind, a deviation variable (ε) can be added to the perfect rectangular pattern in Fig. 3(a) to model the case with an offset rectangle, as in Fig. 4(a). As the offset between points A and C may differ from that between points B and D, it is logical to separate ε into two individual parameters, ε_{AC} and ε_{BD}, which represent the misalignment of the upper and lower parts of the calibration pattern, respectively [Fig. 4(b)]. Note that it is equivalent to separate the length variable (L) into L_{AB} and L_{CD} to represent the different lengths of the left and right lane

0091-3286/2013/$25.00 © 2013 SPIE

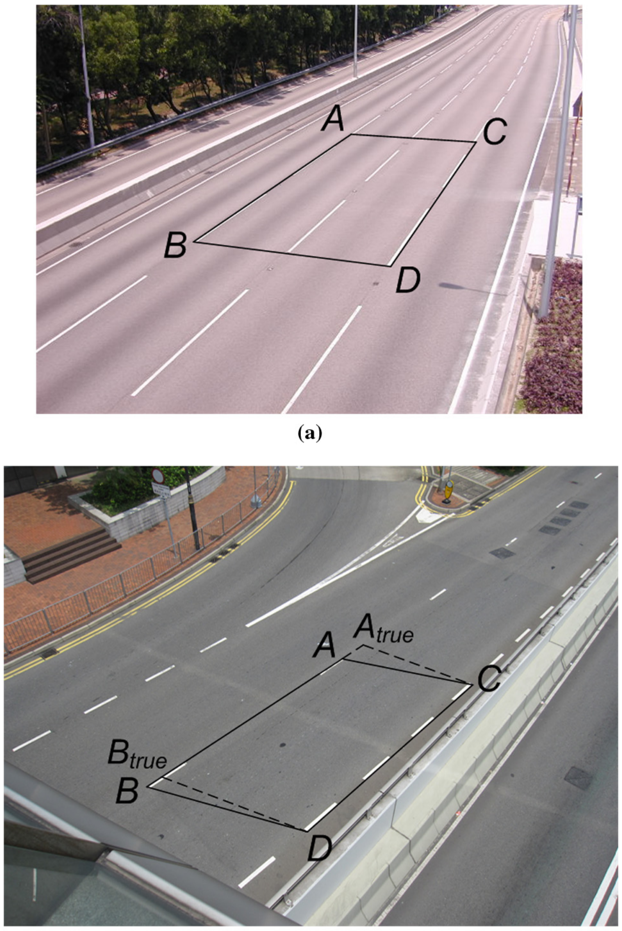

Fig. 1 A rectangular calibration pattern and its limitation (models in Refs. 8 and 9). (a) Rectangular lane marking pattern. (b) Misalignment of lane markings.

Fig. 2 Crosswalk markings form an imperfect rectangle.

markings, respectively. The new calibration model is constructed based on the geometric conditions of the four calibration points, taking these variables into account. The detailed mathematics of the proposed model are discussed in Sec. 4.

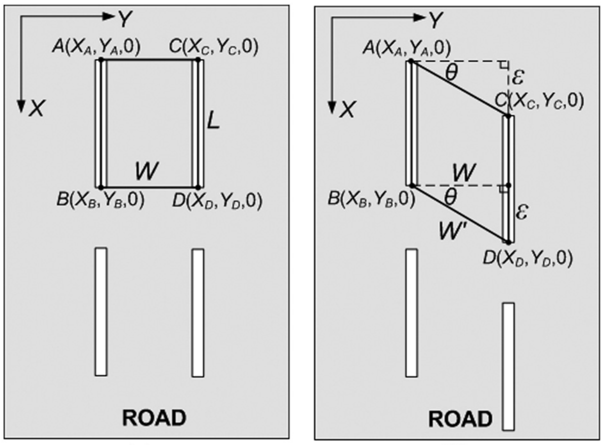

Fig. 3 Rectangle formed by lane markings. (a) Rectangle defined without offset. (b) Offset lane markings.

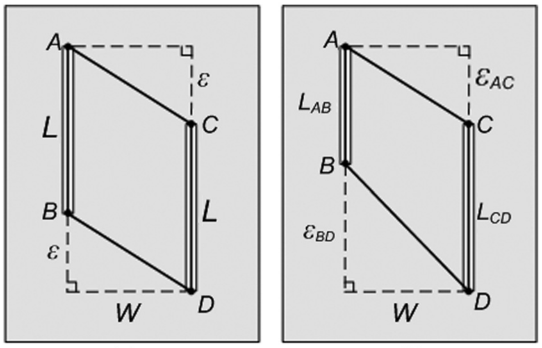

Fig. 4 Degrees of freedom for an imperfect rectangle. (a) Case 1: Misalignment of lane markings. (b) Case 2: Different lengths of lane markings.

3 Related Works

The problem of camera calibration has been intensively investigated in the past few decades in the context of computer vision and the forensic sciences.[10,11] For road traffic applications, researchers have attempted to use various shapes in the 3-D space to develop calibration models that define the most representative relationship between the 2-D and the 3-D space.[8,9,12–18] Selected works with technological significance are discussed below in chronological order.

Fukui[12] used a diamond-shaped calibration pattern placed on a wall to determine the location and horizontal deviation of the camera with respect to the calibration pattern (Fig. 5). The method assumes that the optical center and the calibration pattern must be set at the same height, and the dimensions of the calibration pattern must be known *a priori*. In reality, although diamond-shaped objects may be found on the road, surveillance cameras are usually located at different heights, thus preventing the application of Fukui's model in VTS. Although Courtney et al.[7] relaxed this unilevel restriction, the calibration pattern is still not general enough for real application.

Instead of using man-made patterns, Chou and Tsai[13] used the corner between a wall and a ceiling for their calibration pattern (Fig. 6). The three intersecting lines of the planes form a 'Y-shape,' which varies according to the viewing angle of the camera. The camera parameters can be calculated if the distance between the camera and ceiling is known in advance. In reality, however, although walls and ceilings can be found indoors, they can hardly be found

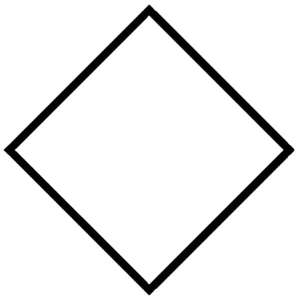

Fig. 5 Diamond-shaped calibration pattern used in Fukui's model.[12]

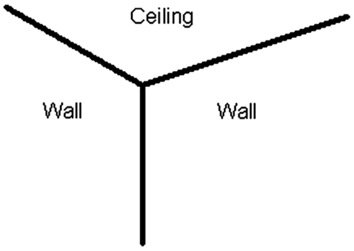

Fig. 6 Wall and ceiling corners used in Chou and Tsai's model.[13]

in road images, thus precluding the application of the model in traffic surveillance.

Tsai[14] proposed using the corners of 16 black squares as calibration points, as depicted in Fig. 7. Perspective projection with pin-hole geometry was used to transform these points for calibration, and optimization techniques such as steepest descent were used to correct lens distortion. The major drawback of this approach is that a large amount of 3-D data (64 corners) has to be handled during calibration, compared with the four corner points used in most methods.[8,9,12] Moreover, as with the previous two models, it is almost impossible to find 16 squares on the road.

Whereas other researchers have focused on using square patterns for calibration, Wang and Tsai[15] were the first to investigate the feasibility of using hexagonal patterns, due to the availability of vanishing points (Fig. 8). Ideally, a vanishing line can be formed when the hexagon is projected from a 3-D image onto a 2-D image. For nonideal cases, a least-squares algorithm can be employed to fit a straight line to the vanishing points, and the camera parameters can be calculated based on the geometric hints of the fitted line. Similar to Tsai's model,[14] the difficulty of finding ideal hexagonal objects on the road means that it is preferable to use simple patterns for calibration, such as rectangles or parallelograms.

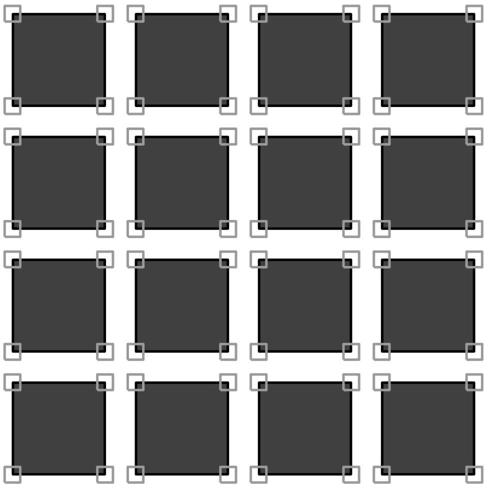

Fig. 7 An array of 16 squares in Tsai's model.[14]

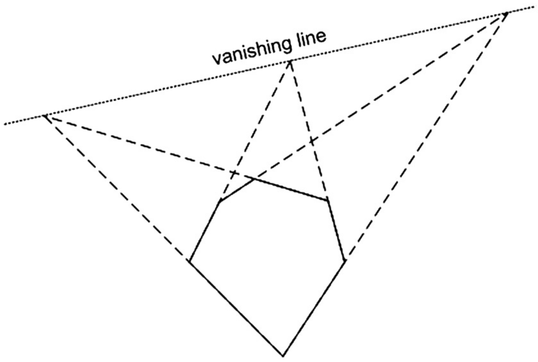

Fig. 8 Hexagonal pattern and vanishing line used in Wang and Tsai's model.[15]

Bas and Crisman[16] initiated the use of road-lane markings for calibration, using the edges of the road shoulder in their calibration model. Four points, *a*, *b*, *c* and *d* were selected arbitrarily from the left and right shoulder (Fig. 9). Assuming that the camera height and tilt angle are known *a priori*, the vanishing point can be used to compute the rest of the camera parameters. The advantage of this model is that it does not require predefined shapes for calibration. The drawback is that in reality, specific camera parameters such as the camera height are not always known in advance, which limits the practicality of the model.

Rather than using fixed objects on the road for calibration, Schoepflin and Dailey[17] identified parallel and perpendicular

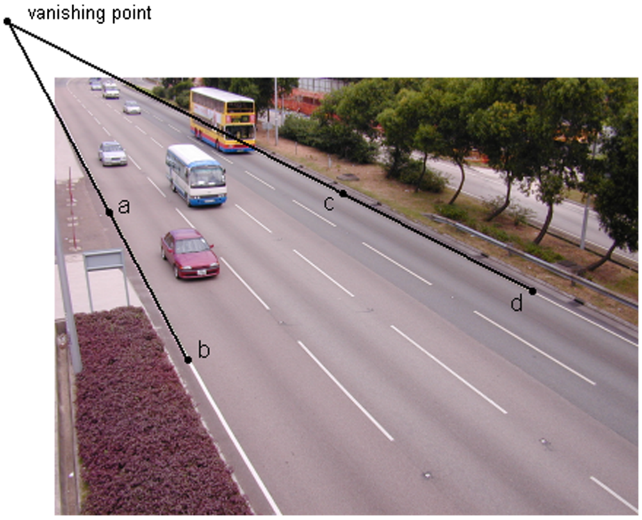

Fig. 9 Defined points of road edges used in Bas and Crisman's model.[16]

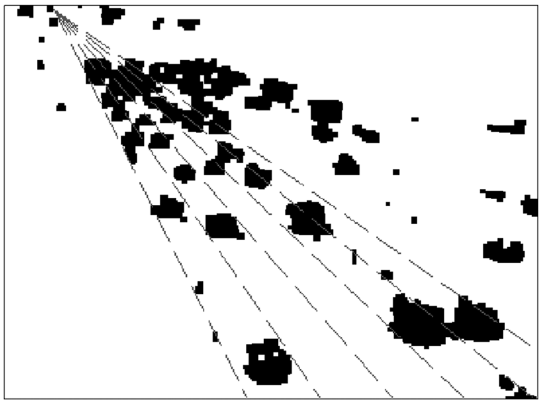

Fig. 10 Activity map used in Schoepflin and Dailey's model.[17]

lines on the road through the analysis of extracted vehicle blobs (Fig. 10). An activity map of the traffic flow is created to identify lines that are parallel to the road direction, and the bottom edges of vehicles are used to identify perpendicular lines. This allows two vanishing points to be formed to compute the camera parameters. The major drawback of this model is that creating an activity map would be inaccurate in situations where vehicles frequently change lanes, thus preventing the application of this method in such situations.

Lai[18] employed a 'H-shape' by drawing two lines along the road-lane direction (pq and rs) with an additional line perpendicular to the road (mn) (Fig. 11). This model is similar to Bas and Crisman's model,[16] with an extra horizontal line (mn) defined by the top or bottom edge of one lane marking. The advantage of this model is that it is capable of determining a more complete set of camera parameters than the aforementioned models. The drawback is that it ignores an important parameter (i.e., the swing angle), which may affect the accuracy of calibration. Moreover, drawing a horizontal line with reference to just one lane marking may result in inaccuracies.

Fung et al.[8] used a rectangular shape defined by road-lane markings to form two vanishing points for calibration (Fig. 12). The model requires the lane width (w), which should be easily obtainable from the road database. This calibration pattern is readily found in road images, and the set of computed camera parameters is the most complete among the above-mentioned models. However, as mentioned in Sec. 2, if two side-by-side road-lane markings are not completely aligned, then a rectangle is unlikely to be formed. Another drawback is that the model depends on two vanishing points. This can create a problem when the camera viewing angle is parallel to the road direction, because one of the vanishing points reaches infinity, leading to serious error in the estimated parameters.

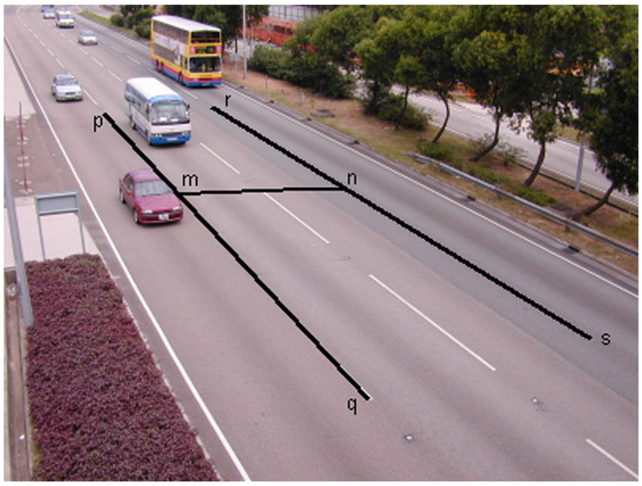

Fig. 11 Defined 'H-shape' used in Lai's model.[18]

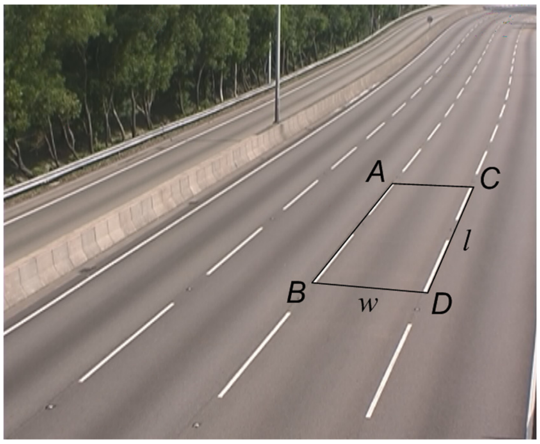

Fig. 12 Defined rectangle used in the Fung et al. model[8] and He and Yung model.[9]

To solve this problem, He and Yung[9] proposed a criterion for selecting only one of the two vanishing points if one of them is approaching infinity, thus reducing the error in parameter estimation. The improved model was shown to yield consistent performance in near-parallel cases. However, an additional piece of information, the length of the lane markings (l), is needed in this model (Fig. 12). Moreover, as with the Fung et al. model,[8] a regular rectangle is required for calibration. This motivates us to refine the model to eliminate this restriction.

4 Proposed Methodology

4.1 *Camera Model*

The generic camera model originally proposed by Fung et al.,[8] based on Haralick's perspective transformation,[19] was adopted as the foundation of the newly proposed camera calibration model. He and Yung[9] improved Fung's camera model by using the camera height (h) instead of the length of the optical axis (l) to make the model more descriptive. As the camera height is a very important quantity in VTS, we adopted the latter version of the camera model as the basis of our development (Fig. 13). Other camera parameters, including the pan angle (p), tilt angle (t), swing angle (s), and focal length (f) remain unchanged.

Let $\mathbf{Q} = (X_Q, Y_Q, Z_Q)$ be an arbitrary point in the 3-D world coordinates, and let $\mathbf{q} = (x_q, y_q)$ be point $\mathbf{Q}$ projected onto the 2-D image coordinates (Fig. 13).[9] The forward projection, which projects point $\mathbf{Q}$ to $\mathbf{q}$ from 3-D to 2-D (i.e., $\mathbf{q} = \Phi\{\mathbf{Q}\}$), can be defined in terms of the camera parameters as:

$$x_q = \frac{f \cdot [X_Q(\cos p \cos s + \sin p \sin t \sin s) + Y_Q(\sin p \cos s - \cos p \sin t \sin s) + Z_Q \cos t \sin s]}{-X_Q \sin p \cos t + Y_Q \cos p \cos t + Z_Q \sin t + h/\sin t}, \tag{1}$$

and

$$y_q = \frac{f \cdot [X_Q(-\cos p \sin s + \sin p \sin t \cos s) + Y_Q(-\sin p \sin s - \cos p \sin t \cos s) + Z_Q \cos t \cos s]}{-X_Q \sin p \cos t + Y_Q \cos p \cos t + Z_Q \sin t + h/\sin t}. \tag{2}$$

The inverse projection, which projects point $\mathbf{q}$ to $\mathbf{Q}$ from 2-D back to 3-D (i.e., $\mathbf{Q} = \Phi^{-1}\{\mathbf{q}\}$), can also be defined in terms of the same set of camera parameters as:

$$X_Q = \frac{h \sin p/\sin t \cdot (x_q \sin s + y_q \cos s) + h \cos p(x_q \cos s - y_q \sin s)}{x_q \cos t \sin s + y_q \cos t \cos s + f \sin t}, \tag{3}$$

and

$$Y_Q = \frac{-h \cos p/\sin t \cdot (x_q \sin s + y_q \cos s) + h \sin p(x_q \cos s - y_q \sin s)}{x_q \cos t \sin s + y_q \cos t \cos s + f \sin t}. \tag{4}$$

In Eqs. (3) and (4), it is assumed that the 3-D coordinate of point $\mathbf{Q}$ lies on the ground for calibration purposes (i.e., $Z_Q = 0$). For real transformation, it is necessary to include the expression Φ^{-1}, which includes the case of $Z_Q \neq 0$, because an image point $\mathbf{q} = (x_q, y_q)$ does not always represent a point on the ground but may be the height of a person's head or the roof of a vehicle. For the transformation where $Z_Q \neq 0$, please refer to Appendix A1.

4.2 *Proposed Camera Calibration Methodology*

Based on the camera model described in the previous section, in this section, we introduce and develop the proposed camera calibration model. For the detailed proofs of the mathematics and equations, please refer to Appendices A1 to A4. First, in our model, the X-axis is defined along the direction of the road in the 3-D world coordinate system, and the Y-axis is defined as the axis that is perpendicular to the road direction (Fig. 14). It is assumed that the road surface is flat and is represented by the X-Y world plane at $Z = 0$. It is also assumed that the road under surveillance is reasonably straight and the lane markings approximate straight lines and are almost parallel to each other.

The four corner points used for calibration are A, B, C, and D, with world coordinates $(X_A, Y_A, 0)$, $(X_B, Y_B, 0)$, $(X_C, Y_C, 0)$ and $(X_D, Y_D, 0)$, respectively. AB and CD are the lane markings of the left-hand and right-hand side, respectively. Considering the parallelogram or trapezoidal patterns discussed in Sec. 2 [Fig. 4(a) and 4(b)], the adopted variables in the model are first, L_{AB} and L_{CD}, which represent the length of the left and right lane markings, respectively, second, ε_{AC} and ε_{BD}, which represent the deviation of the two top corners and the two bottom corners of the lane markings, respectively, and third, W, which represents the lane width (Fig. 14).

4.2.1 *Calibration conditions*

With the above-mentioned settings, the new calibration model is designed to allow the computation of the camera parameters from the length of lane markings (L_{AB} and L_{CD}) and the lane width (W). These variables can easily be obtained from the road using simple surveying devices or from specifications. To allow comparison with the models in Refs. 8 and 9, five conditions are modeled based on the geometrical properties of the calibration points and variables, as depicted in the first column of Table 1. For comparative purposes, the conditions of the Fung et al.[8] and He and Yung[9] models are shown in the two right-hand

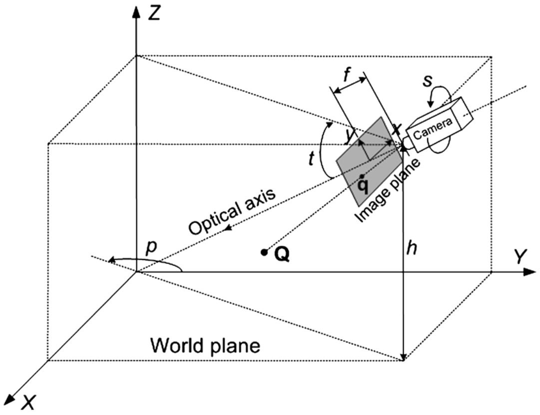

Fig. 13 Adopted camera model.

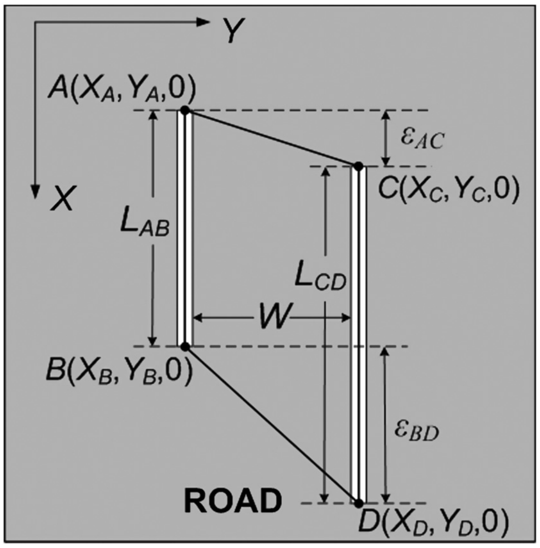

Fig. 14 Variables in the new camera calibration model.

Table 1 Calibration conditions.

	New model	Fung et al.[8]	He and Yung[9]
Condition 1	(5)	$Y_A = Y_B$	$Y_A = Y_B$
Condition 2	(6)	$Y_C = Y_D$	$Y_C = Y_D$
Condition 3	(7)	$X_A = X_C$	$X_B - X_A = L$
Condition 4	(8)	$X_B = X_D$	$X_D - X_C = L$
Condition 5	(9)	$Y_C - Y_A = W$	$Y_C - Y_A = W$

$$Y_A = Y_B \tag{5}$$

$$Y_C = Y_D \tag{6}$$

$$X_B - X_A = L_{AB} \tag{7}$$

$$X_D - X_C = L_{CD} \tag{8}$$

$$Y_C - Y_A = W \tag{9}$$

columns of Table 1. It can be seen from the table that conditions 1, 2 and 5 [i.e., Eqs. (5), (6), and (9)] are the same for all three models, whereas conditions 3 and 4 [i.e., Eqs. (7) and (8)] vary substantially in the new model.

4.2.2 *Assumptions of the model*

The camera parameters mentioned in Sec. 4.1 (i.e., p, t, s, f and h) can be determined by conditions 1 to 5 [i.e., Eqs. (5) through (9)] with the inverse projection (Φ^{-1}) [i.e., Eqs. (3) and (4)]. A detailed description of the method used to determine these parameters is provided in the following subsection. The assumptions of the calibration model used in Ref. 9 are also applied here; i.e., $\{s, t, f, p, h\}$, $\{s + \pi, t, -f, p, h\}$ and $\{s, t, f, p + \pi, -h\}$ are sets of equivalent solutions. However, the constraints $f > 0$, $h > 0$ and $-\pi/2 < t < 0$ are imposed to reflect the physical configuration of the camera in real situations. Therefore, the only acceptable set of parameters is $\{s, t, f, p, h\}$.

4.2.3 *Case 1: trapezoidal case*

To obtain the camera parameters when the calibration pattern is a trapezoid, the length of the two lane markings that define the trapezoid (i.e., L_{AB} and L_{CD}), and the width between the two lane markings (W) are needed (Fig. 14). These dimensions can be obtained with simple surveying devices, or from specifications or databases if they are available. Assume that L_{AB} and L_{CD} are obtainable, and if $L_{AB} \neq L_{CD}$ then the numeric solution for the swing angle (s) can be obtained by the following optimization equation:

$$\arg\min_{s} \left|(-\kappa_1 + \kappa_3) + \left(\sqrt{\kappa_1^2 - 4\kappa_2} - \sqrt{\kappa_3^2 - 4\kappa_4}\right)\right|, \tag{10}$$

where $\kappa_1 = \frac{L_{AB}}{W} \cdot \frac{\beta_{ABC,CAB} - \nu_{AB} \cdot \alpha_{ABC,CAB}}{\alpha_{ABC,BAC}}$, $\kappa_2 = \frac{\nu_{AB} \cdot \beta_{ABC,BAC}}{\alpha_{ABC,BAC}}$, $\kappa_3 = \frac{L_{CD}}{W} \cdot \frac{\beta_{ADC,CAD} - \nu_{AB} \cdot \alpha_{ADC,CAD}}{\alpha_{CDA,DAC}}$, and $\kappa_4 = \frac{\nu_{AB} \cdot \beta_{CDA,DAC}}{\alpha_{CDA,DAC}}$.

The primitive variables ν, α, and β are defined as

$$\nu_{AB} = \frac{(\Lambda_A - \Lambda_B)\varphi}{\Gamma_A \Lambda_B - \Gamma_B \Lambda_A + (\Gamma_A - \Gamma_B)\varphi},$$

$\alpha_{\langle e\rangle\langle f\rangle\langle g\rangle,\langle h\rangle\langle i\rangle\langle j\rangle} = \Gamma_{\langle e\rangle}(\Lambda_{\langle f\rangle} + \varphi)(\Lambda_{\langle g\rangle} + \varphi) - \Gamma_{\langle h\rangle}(\Lambda_{\langle i\rangle} + \varphi)(\Lambda_{\langle j\rangle} + \varphi)$, and $\beta_{\langle e\rangle\langle f\rangle\langle g\rangle,\langle h\rangle\langle i\rangle\langle j\rangle} = \Lambda_{\langle e\rangle}(\Lambda_{\langle f\rangle} + \varphi)(\Lambda_{\langle g\rangle} + \varphi) - \Lambda_{\langle h\rangle}(\Lambda_{\langle i\rangle} + \varphi)(\Lambda_{\langle j\rangle} + \varphi)$.

For example, $\alpha_{ABC,BAC} = \Gamma_A(\Lambda_B + \varphi)(\Lambda_C + \varphi) - \Gamma_B(\Lambda_A + \varphi)(\Lambda_C + \varphi)$, and $\beta_{ABC,CAB} = \Lambda_A(\Lambda_B + \varphi)(\Lambda_C + \varphi) - \Lambda_C(\Lambda_A + \varphi)(\Lambda_B + \varphi)$.

The elementary variables Λ_Q, Γ_Q, and φ are defined as:

$$\Lambda_Q = x_q \sin s + y_q \cos s, \qquad \Gamma_Q = x_q \cos s - y_q \sin s,$$

and

$$\varphi = -\frac{(\Gamma_A \Lambda_B - \Gamma_B \Lambda_A)(\Lambda_C - \Lambda_D) - (\Gamma_C \Lambda_D - \Gamma_D \Lambda_C)(\Lambda_A - \Lambda_B)}{(\Gamma_A - \Gamma_B)(\Lambda_C - \Lambda_D) - (\Gamma_C - \Gamma_D)(\Lambda_A - \Lambda_B)}.$$

Once we have the swing angle (s), the tilt angle (t) can be calculated by:

$$t = \sin^{-1}\left(\frac{-\kappa_1 \pm \sqrt{\kappa_1^2 - 4\kappa_2}}{2}\right), \tag{11}$$

where $\pm$ is chosen such that $-1 < (-\kappa_1 \pm \sqrt{\kappa_1^2 - 4\kappa_2})/2 < 0$, because t is bounded by $-\pi/2$ and 0 according to the condition stated in Sec. 4.2.2, and an arcsine with a value greater than 1 or smaller than -1 is meaningless.

The pan angle (p) can be computed in terms of t by:

$$p = \tan^{-1}\left(\frac{\nu_{AB}}{\sin t}\right), \tag{12}$$

where the definition of ν_{AB} is the same as that in Eq. (10).

Focal length (f) can be calculated as:

$$f = \frac{\varphi}{\tan t}, \tag{13}$$

and if $f < 0$, then $f = -f$ and $s = s + \pi$.

Finally, the camera height (h) can be computed as follows:

$$h = \frac{W \sin t \cos t}{\cos p} \times \left(\frac{\Gamma_C \tan p \sin t - \Lambda_C}{\Lambda_C + \varphi} - \frac{\Gamma_A \tan p \sin t - \Lambda_A}{\Lambda_A + \varphi}\right)^{-1}, \tag{14}$$

and if $h < 0$, then $h = -h$ and $p = p + \pi$.

This gives a complete solution for the whole set of camera parameters $\{s, t, f, p, h\}$ from the four defined points in the image, i.e., $\mathbf{q} = \{(x_q, y_q) | q \in a, b, c, d\}$, the lane width ($W$), and the length of the lane markings (L_{AB} and L_{CD}).

4.2.4 *Case 2: parallelogram case*

If the calibration pattern is a parallelogram, then $L_{AB} = L_{CD}$ and $\varepsilon_{AC} = \varepsilon_{BD}$. In such a case, the swing angle (s) can be obtained by the following closed-form equation:

$$s = \tan^{-1}\left[\frac{(\varsigma_{4,2,3,1} - \varsigma_{3,2,4,1} + \varsigma_{1,4,2,3} - \varsigma_{4,2,1,3} + \varsigma_{3,2,1,4} - \varsigma_{1,3,2,4} + \varsigma_{1,3,4,2} - \varsigma_{1,4,3,2})}{(\upsilon_{4,2,3,1} - \upsilon_{3,2,4,1} + \upsilon_{1,4,2,3} - \upsilon_{4,2,1,3} + \upsilon_{3,2,1,4} - \upsilon_{1,3,2,4} + \upsilon_{1,3,4,2} - \upsilon_{1,4,3,2})}\right], \tag{15}$$

where $\varsigma_{\langle a\rangle,\langle b\rangle,\langle c\rangle,\langle d\rangle} = \gamma_{\langle a\rangle}\gamma_{\langle b\rangle}\chi_{\langle c\rangle}\zeta_{\langle d\rangle}$ and $\upsilon_{\langle a\rangle,\langle b\rangle,\langle c\rangle,\langle d\rangle} = \chi_{\langle a\rangle}\chi_{\langle b\rangle}\gamma_{\langle c\rangle}\zeta_{\langle d\rangle}$; '1' represents AB, '2' represents CD, '3' represents AC, and '4' represents BD. For example, $\varsigma_{4,2,3,1} = \gamma_{BD}\gamma_{CD}\chi_{AC}\zeta_{AB}$ and $\upsilon_{3,2,4,1} = \chi_{AC}\chi_{CD}\gamma_{BD}\zeta_{AB}$, etc. Moreover, $\chi_{PQ} = x_q - x_p$, $\gamma_{PQ} = y_q - y_p$, and $\zeta_{PQ} = x_p y_q - x_q y_p$.

The remaining camera parameters, including t, p, f, and h, can be calculated by Eqs. (11)–(14), respectively.

4.2.5 *Case 3: rectangular case*

The newly proposed calibration model is essentially a generalized version of the models in Refs. 8 and 9. In another words, both of these models are particular cases of our generalized model, which exploits a rectangle for calibration. Therefore, $L_{AB} = L_{CD} = L$ and $\varepsilon_{AC} = \varepsilon_{BD} = 0$, hence the tilt angle ($t$) can be computed by:

$$t = \sin^{-1}\left(-\sqrt{-\nu_{AC}\nu_{AB}}\right), \tag{16}$$

where $\nu_{PQ} = (\Lambda_P - \Lambda_Q)\varphi/[\Gamma_P\Lambda_Q - \Gamma_Q\Lambda_P + (\Gamma_P - \Gamma_Q)\varphi]$, and the definitions of Λ_{PQ}, Γ_{PQ} and φ are the same as in Sec. 4.2.3.

The remaining camera parameters, including s, p, f, and h, can be computed by Eqs. (12)–(15), respectively, and the only information required for calibration is W.

4.2.6 *Summary of each case*

In summary, trapezoid, parallelogram, or rectangular shapes can be used for calibration with the new model. For a trapezoid, the camera parameters $\{s, t, f, p, h\}$ can be determined using L_{AB}, L_{CD}, and W with Eqs. (10) through (14), respectively. In the case of a parallelogram, AC and BD are parallel to each other but not necessarily to the Y axis, in which case the camera parameters can be computed using L and W with Eqs. (15) and (11) through (14), respectively. Finally, for a rectangle, the model is the same as the Fung and He models, in which the camera parameters can be determined by W with Eqs. (15), (16) and (12) to (14), respectively.

5 Results and Discussion

The proposed methodology was tested in both a laboratory and a real-world environment to establish the accuracy of camera parameter extraction. In the laboratory, bricks were placed on the floor as a reference point. Trapezoid- or parallelogram-shaped pieces of paper were glued onto the floor to form the four corner points, A, B, C and D of the calibration pattern [Fig. 15(b)]. Test objects such as paper boxes were placed in the scene for testing the accuracy of calibration, and various points were chosen to form a set of test lengths for the evaluation of accuracy [Fig. 15(c)].

Images of the scene were taken by a digital camera (Canon IXUS 870 IS) and transferred to a desktop for further analysis [Fig. 15(a)]. The dimensions of the calibration pattern, i.e., L_{AB}, L_{CD} and W, and the set of test lengths were measured by ruler and recorded by hand. The 2-D coordinates of the four calibration points were then recorded from the image, and the camera parameters were computed according to the proposed methodology, as described in Sec. 4.2. To test the accuracy of calibration, the image coordinates of the test points were transformed from 2-D to 3-D world coordinates by Eqs. (3) and (4) using the extracted camera parameters. This allowed the experimental lengths of these test lines to be computed from the Euclidean distance between two points in the 3-D world coordinates.

To act as the control experiment, additional markings were chosen to form a rectangular shape for calibration [e.g., points A, F, G and D in Fig. 15(b)]. The dimensions of the rectangle (i.e., W' and L') were again measured by ruler, and the camera parameters were computed using the Fung et al.[8] and He and Yung[9] models to allow comparison with the proposed model.

For the outdoor experiments, road scenes that included patterns such as box-markings or crosswalk markings were taken by digital camera [Fig. 17(a)]. These patterns do not usually form perfect or accurate rectangles, thus the only available patterns for calibration tend to be trapezoids, near-parallelograms, or imperfect rectangles. Points A, B, C and D were chosen to form the imperfect pattern for calibration, similar to the one in Fig. 17(b), using the proposed method. For the control experiment, four additional points [e.g., points E, F, G and H in Fig. 17(b)] were chosen to form a rectangle for calibration using the Fung et al.[8] and He and Yung[9] models.

The dimensions of the calibration and control patterns (i.e., L_{AB}, L_{CD}, W, W' and L') were measured with a Leica Total Station, an electronic optical surveying instrument. It is well known that the Total Station can extract the coordinates of points with a high degree of accuracy. This device can record the distance and direction of each point from the reference point, so that the distance between two points can be calculated by a simple cosine rule. The camera parameters can then be computed from this calibration information.

To evaluate the accuracy of the outdoor trial, points were chosen from the markings and objects on the ground, such as a drainage cover, parking space markings, a railway track, and even vehicles on the road. The baseline dimensions of these reference lengths were measured by Total Station, or by referring to specifications such as the railway gauge or the dimensions of vehicles. Similar to the indoor experiment, the lengths of these reference lines were estimated by the extracted camera parameters, and the percentage accuracies were computed and analyzed. The experimental results of the aforementioned trials are discussed in detail below. For details of the ground truth and experimental values, please refer to Tables 2 to 6 in Appendix A5.

5.1 *Indoor, Nonparallelogram*

The first set of images contained a tetrahedron with a pair of parallel lines and a pair of nonparallel lines, referred to here as the 'nonparallelogram' calibration pattern [Fig. 15(a)]. Two tiny paper strips were stuck onto two bricks in the top-right and bottom-left corners representing points G

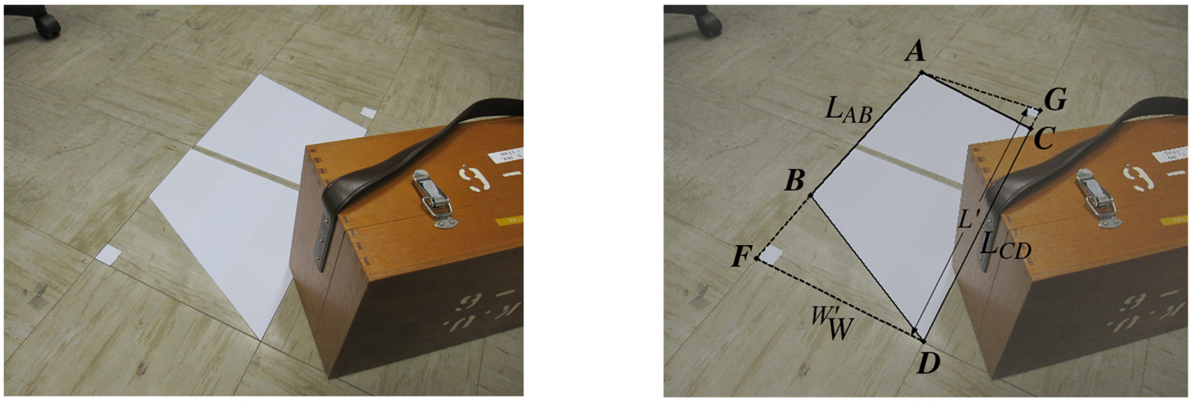

(a)

(b)

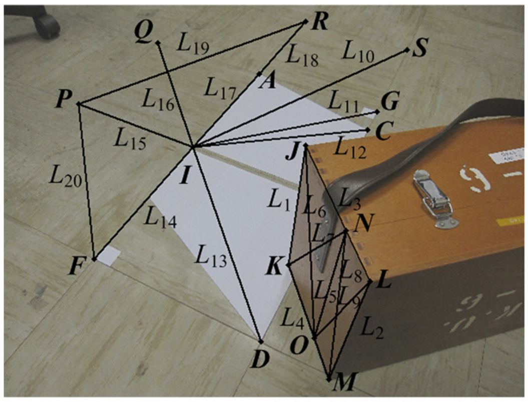

(c)

Method	s (deg)	t (deg)	p (deg)	f (pixels)	h (cm)	μ (%)	σ (%)
Ref. 8 **(*AFGD*)**	3.84	-50.01	113.15	2923.17	60.03	98.93	1.195
Ref. 9 **(*AFGD*)**	3.84	-50.06	113.17	2918.67	59.98	98.91	1.260
Proposed **(*ABCD*)**	3.83	-49.96	113.18	2933.85	60.17	98.99	1.177

(d)

Fig. 15 Indoor nonparallelogram. (a) Image taken; (b) calibration pattern; (c) test lengths; and (d) computed camera parameters and percentage accuracy of length extraction.

and F, respectively, which created rectangle $AFGD$ for the control experiment [Fig. 15(b)]. In Fig. 15(b), note that lines AB and CD form L_{AB} and L_{CD}, line FD forms W and W', and line GD forms L'.

The camera parameters extracted by the models in Refs. 8 and 9 and the proposed method are depicted in Fig. 15(d). As shown in the table, the three methods produced similar swing and tilt angles. The obtained pan angle seems reasonable, as according to the image it should be larger than 90-deg if the view from the left side represents 0-deg. The photos were taken from a height of around 60 cm, and all three methods were capable of extracting this value.

To evaluate the accuracy, a wooden box was placed along the right edge of the calibration pattern [Fig. 15(c)] and twenty test lengths (L_1 to L_{20}) were chosen for evaluation. The experimental lengths were extracted by the aforementioned method of coordinate transformation and Euclidean distance computation. The mean percentage accuracy and standard deviation of each method were computed and shown in the right two columns of Fig. 15(d). All three methods produced highly accurate length estimates with mean accuracy of around 98.9%, although the proposed method produced the highest mean accuracy (i.e., 99.0%). The overall accuracy is >96% for all three methods except for one trial.

5.2 *Indoor, Trapezoidal Pattern*

The second set of images contained a trapezoidal pattern, $ABCD$, taken in a laboratory environment [Fig. 16(a)]. Two additional points, G and H, were marked to form the rectangle $ABGH$ for the control experiment; note that L' and L_{AB} are formed by points A and B, W' and W are formed by points B and H, and L_{CD} is formed by points C and D [Fig. 16(b)].

Figure 16(d) shows that the extracted swing angles of all three models are around 4-deg, which agrees with each other. The tilt angles computed by the model in Ref. 9 and the proposed method are around −51.2-deg, whereas the angle computed by the model in Ref. 8 is slightly offset as −53.11-deg. The obtained pan angle is around 71-deg for all three methods, which seems reasonable as the pan angle should be smaller than 90-deg according to the image. For height estimation, the ground truth is 54 cm; both the model in Ref. 9 and the proposed model accurately estimated this value, but the estimate of the model in Ref. 8 was about 2 cm less than the measured value.

Accuracy was evaluated by placing three boxes around the calibration pattern. The percentage accuracies are shown in the right two columns of Fig. 16(d). The performance of the model in Ref. 8 was not as good as that of the model in Ref. 9 or the proposed model: the mean accuracy was 98.2% for the model in Ref. 8, 98.7% for both the model in Ref. 9, and 98.6% for the proposed model. It is likely that the model in Ref. 8 suffers from the problem of ill-conditioning when the pan angle is closer to 90-deg than to 0-deg, thus reducing its accuracy. However, neither the model in Ref. 9 nor the proposed model suffer from this problem.

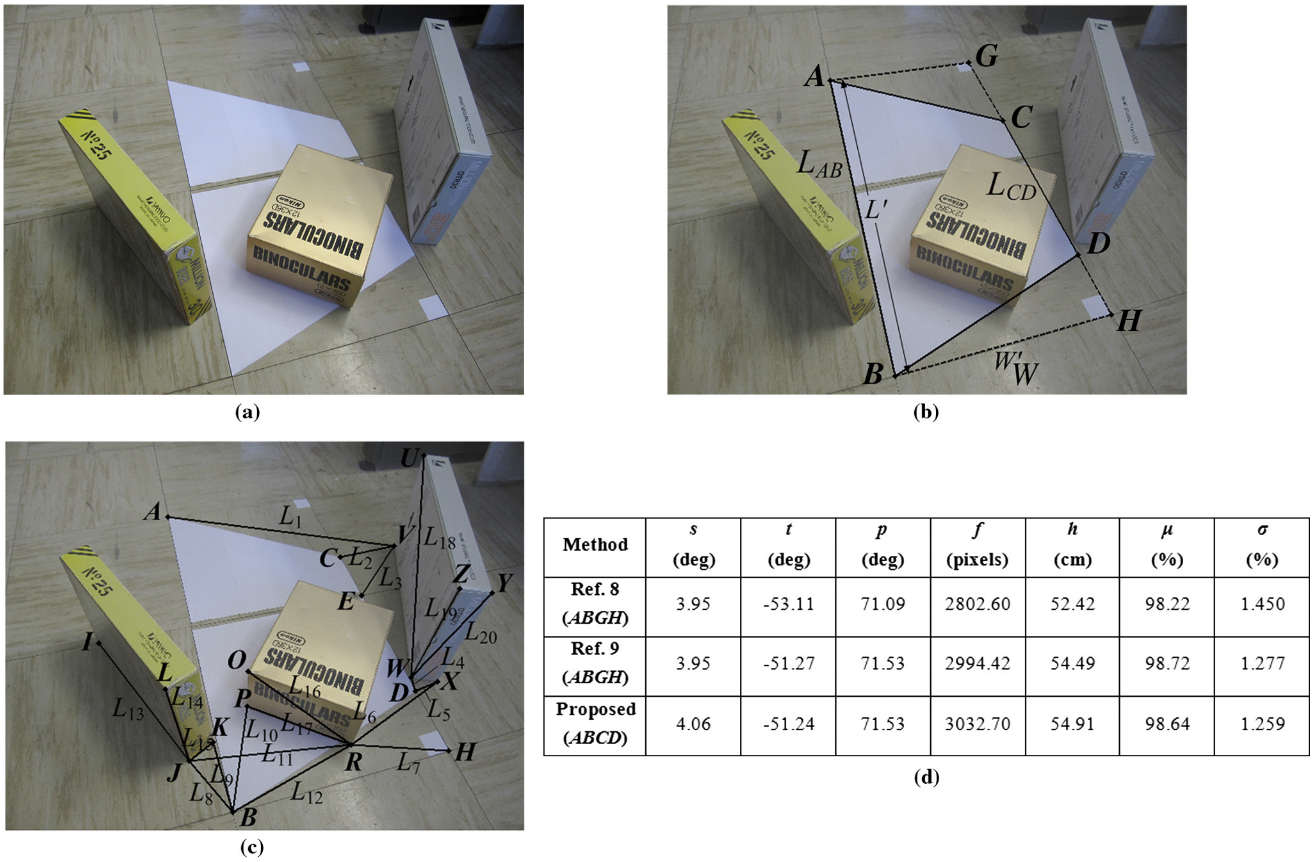

(a) (b) (c)

Method	s (deg)	t (deg)	p (deg)	f (pixels)	h (cm)	μ (%)	σ (%)
Ref. 8 (*ABGH*)	3.95	-53.11	71.09	2802.60	52.42	98.22	1.450
Ref. 9 (*ABGH*)	3.95	-51.27	71.53	2994.42	54.49	98.72	1.277
Proposed (*ABCD*)	4.06	-51.24	71.53	3032.70	54.91	98.64	1.259

(d)

Fig. 16 Indoor trapezoidal pattern. (a) Image taken; (b) calibration pattern; (c) test lengths; and (d) computed camera parameters and percentage accuracy of length extraction.

5.3 *Outdoor, Trapezoidal Pattern*

The third set of images contained box-markings taken in a parking lot area [Fig. 17(a)]. However, the corners of the box-markings did not form a perfect rectangle, as the outline of the box contained more than four corners. Therefore, points A, B, C and D were chosen to be the corners of the calibration pattern, forming a trapezoid in which line AB is parallel to line CD, and lines AC and BD are not parallel to each other [Fig. 17(b)]. Consequently, W does not correspond to the length of BD, as BD is not perpendicular to lines AB and CD. Therefore, W should be measured as the horizontal distance between L_{AB} and L_{CD} by constructing a horizontal line between these two lines. Points E, F, G and H were chosen to form a rectangle with dimension L' and W' for the control experiment [Fig. 17(b)]. Although they do not form an ideal rectangle, they serve as the calibration pattern for the models found in Refs. 8 and 9.

The computed camera parameters are shown in Fig. 17(d). The pan angle computed by the models in Refs. 8 and 9 is around 101-deg and the angle computed by the newly proposed model is 55.82-deg. This difference is to be expected, because the patterns used in the models have different orientations, as can be seen in Fig. 17(b). However, both values are consistent with their own pattern, which should be smaller than 90-deg for trapezoid $ABCD$, but larger than 90-deg for rectangle $EFGH$. According to the Total Station measurement, the ground truth camera height is around 534 cm, which is very close to the height estimated by the proposed model (i.e., 533.27 cm).

In terms of accuracy, the model in Ref. 8 is generally less accurate than that of the model in Ref. 9 and the new model, with one estimated value even lower than 95%. Again, this is probably due to the ill-condition problem in the model in Ref. 8. Neither the model in Ref. 9 nor the new model has this problem, with mean accuracies of 98.7% and 98.8%, respectively [Fig. 17(d)]. However, a considerable drawback of the model in Ref. 9 is that it cannot use a trapezoid as the calibration pattern; hence, it would be unable to extract the camera parameters and would be unable to estimate the test lengths accurately if the road did not feature a rectangular pattern. This situation will become apparent in the subsequent two examples.

5.4 *Outdoor, Close to Parallelogram*

The fourth set of images was taken in a crosswalk area with a shape close to a parallelogram [Fig. 18(a)]. It is not strictly a parallelogram as the markings at point A are worn, which means that line AC is not completely parallel to line BD [Fig. 18(b)]. For the control experiment, there were no points to form a perfect rectangle, except around the two drainage covers at the far end of the pavement, which formed a tiny rectangle $EFGH$. It is highly unlikely that such a small pattern would provide accurate calibration, as accuracy would be seriously compromised by pixel error. However, it is the only choice in this case.

The computed camera parameters in Fig. 18(d) indicate that the models found in Refs. 8 and 9 produced quite similar swing angle and focal length estimations, and these are quite

Table 2 Extracted lengths for the indoor nonparallelogram case (Sec. 5.1).

Trial	Line	End points	Real length (cm)	New model (cm)	Model in Ref. 9 (cm)	Model in Ref. 8 (cm)
1	L_1	*AV*	47.0	46.3	46.6	46.7
2	L_2	*CV*	12.5	12.0	12.1	12.1
3	L_3	*EV*	16.5	16.6	16.7	16.4
4	L_4	*DW*	2.2	2.3	2.3	2.3
5	L_5	*DX*	4.1	4.2	4.2	4.3
6	L_6	*RX*	18.5	18.2	18.2	18.1
7	L_7	*RH*	14.0	13.5	13.5	13.6
8	L_8	*JB*	8.8	8.8	8.8	8.8
9	L_9	*KB*	10.0	9.6	9.6	9.5
10	L_{10}	*PB*	14.8	14.8	14.7	14.4
11	L_{11}	*JR*	21.5	22.0	22.1	22.1
12	L_{12}	*BR*	18.2	18.2	18.2	18.2
13	L_{13}	*IJ*	25.5	25.0	25.0	24.8
14	L_{14}	*LJ*	18.0	18.2	18.3	18.8
15	L_{15}	*JK*	4.0	4.0	4.0	4.0
16	L_{16}	*OR*	17.2	17.9	17.9	18.0
17	L_{17}	*PR*	15.2	15.5	15.5	15.5
18	L_{18}	*UW*	37.2	37.1	37.2	36.5
19	L_{19}	*ZW*	19.5	19.2	19.2	19.3
20	L_{20}	*YW*	19.9	19.6	19.5	19.4
21	L_{AB}	*AB*	61.0	60.8	61.0	59.8
22	L_{CD}	*CD*	31.0	31.0	31.1	30.5
23	L_{AC}	*AC*	36.5	36.2	36.4	36.4
24	L_{BD}	*BD*	32.0	32.2	32.2	32.0
25	L_{AD}	*AD*	59.3	58.9	59.2	58.8
26	L_{CB}	*CB*	50.9	51.4	51.5	50.5
27	L_{GH}	*GH*	61.0	60.7	61.0	59.8
28	L_{AG}	*AG*	30.5	30.3	30.5	30.5
29	L_{BH}	*BH*	30.5	30.5	30.5	30.5
30	L_{AH}	*AH*	68.0	67.5	67.8	67.1
31	L_{GB}	*GB*	68.0	68.4	68.6	67.1

Table 3 Extracted lengths for the indoor trapezoidal case (Sec. 5.2).

Trial	Line	End points	Real length (cm)	New model (cm)	Model in Ref. 9 (cm)	Model in Ref. 8 (cm)
1	L_1	*JK*	26.3	26.5	26.6	26.6
2	L_2	*LM*	26.3	26.8	26.8	26.8
3	L_3	*JL*	19.5	18.7	18.5	18.6
4	L_4	*KM*	19.5	18.9	18.9	18.9
5	L_5	*NO*	26.3	26.8	26.8	26.8
6	L_6	*JO*	29.1	29.6	29.6	29.6
7	L_7	*NK*	29.1	29.6	29.6	29.6
8	L_8	*NM*	26.6	27.5	27.5	27.5
9	L_9	*LO*	26.6	27.4	27.4	27.4
10	L_{10}	*IS*	68.1	68.1	68.2	68.2
11	L_{11}	*IG*	43.1	43.2	43.3	43.3
12	L_{12}	*IC*	38.1	38.3	38.4	38.4
13	L_{13}	*ID*	43.1	43.1	43.1	43.1
14	L_{14}	*IF*	30.5	30.4	30.4	30.4
15	L_{15}	*IP*	30.5	29.8	29.8	29.8
16	L_{16}	*IQ*	43.0	42.2	42.2	42.3
17	L_{17}	*IA*	30.5	30.6	30.6	30.6
18	L_{18}	*AR*	30.5	30.5	30.6	30.6
19	L_{19}	*PR*	68.2	68.4	68.4	68.4
20	L_{20}	*PF*	43.0	42.4	42.3	42.4
21	L_{AB}	*AB*	45.8	45.9	45.9	45.9

Table 3 (*Continued*).

Trial	Line	End points	Real length (cm)	New model (cm)	Model in Ref. 9 (cm)	Model in Ref. 8 (cm)
22	L_{CD}	CD	53.5	53.5	53.5	53.5
23	L_{AC}	AC	31.3	31.4	31.4	31.5
24	L_{BD}	BD	34.0	34.3	34.3	34.3
25	L_{AD}	AD	68.0	68.2	68.2	68.2
26	L_{CB}	CB	49.0	49.2	49.2	49.2
27	L_{AF}	AF	61.0	61.0	61.0	61.0
28	L_{GD}	GD	61.0	61.0	61.0	61.0
29	L_{AG}	AG	30.5	30.5	30.5	30.5
30	L_{FD}	FD	30.5	30.5	30.5	30.5
31	L_{GF}	GF	68.0	68.2	68.2	68.2

Table 4 Extracted lengths for the outdoor trapezoidal case (Sec. 5.3).

Trial	Line	End points	Real length (cm)	New model (cm)	Model in Ref. 9 (cm)	Model in Ref. 8 (cm)
1	L_1	IJ	187.0	184.1	183.0	180.0
2	L_2	MN	231.2	232.1	230.6	227.4
3	L_3	OP	238.1	236.7	235.3	232.6
4	L_4	QR	439.4	424.6	418.0	420.4
5	L_5	ST	114.6	113.2	112.9	108.6
6	L_6	UV	198.4	198.3	198.3	198.0
7	L_7	WZ	198.8	198.6	198.6	195.8
8	L_8	A_1A_2	199.6	202.5	198.3	196.2
9	L_9	B_1B_2	95.1	95.2	93.3	91.9
10	L_{10}	C_1C_2	40.2	40.4	41.9	42.0
11	L_{11}	D_1D_2	54.3	52.8	52.8	54.5
12	L_{12}	E_1E_2	72.0	72.1	70.6	72.0
13	L_{13}	F_1F_2	20.0	20.7	20.7	20.6
14	L_{14}	KL	186.4	184.3	183.3	180.7
15	L_{15}	G_1G_2	200.5	197.1	196.0	195.0
16	L_{16}	H_1H_2	99.0	97.1	96.6	97.7
17	L_{17}	I_1I_2	58.0	57.0	56.1	56.5
18	L_{18}	J_1H	279.2	284.1	279.9	274.1
19	L_{19}	K_1K_2	461.4	469.5	459.8	445.0
20	L_{20}	K_1K_3	281.0	284.4	280.0	277.9
21	L_{AB}	AB	427.4	432.7	426.1	417.0
22	L_{CD}	CD	250.3	252.1	250.3	257.6
23	L_{AC}	AC	1156.3	1146.3	1142.9	1144.1
24	L_{BD}	BD	1120.4	1111.8	1105.3	1138.7
25	L_{AD}	AD	1198.1	1185.1	1185.1	1196.5
26	L_{CB}	CB	1170.5	1171.1	1158.5	1173.7
27	L_{EF}	EF	419.0	427.3	418.4	413.7
28	L_{GH}	GH	417.8	427.3	418.4	418.7
29	L_{EG}	EG	198.4	198.1	198.1	193.2
30	L_{FH}	FH	197.7	198.1	198.1	197.6
31	L_{EH}	EH	460.6	471.0	461.3	449.8
32	L_{GF}	GF	465.3	471.0	464.5	469.5

different from the estimates computed by the new model. This inaccuracy could be due to the small size of the calibration pattern, $EFGH$. The new model accurately estimated the ground truth height value of 665.6 cm, although the models in Refs. 8 and 9 were less accurate [Fig. 18(d)].

Twenty test lengths were chosen from the crosswalk, pavement settings, or the height of vehicles (e.g., L_7, L_{14} and L_{10}, respectively) [Fig. 18(c)]. Models in Refs. 8 and 9 both produced very poor length estimates, with most trials between 65% and 85% accurate and a mean accuracy of around 82% [Fig. 18(d)]. The inaccuracy is solely due to the small calibration pattern. However, this is unavoidable as the models in Refs. 8 and 9 can only use rectangles for their calibration patterns, and rectangle $EFGH$ was the only pattern that could be found in this case. The new model overcomes this drawback as it can use one of the many trapezoidal patterns in the scene for calibration. Therefore, accuracy was very high, with a mean of 96.6% [Fig. 18(d)].

5.5 *Outdoor, Imperfect Rectangle*

The fifth set of images was taken at a light rail transit intersection. As the box-markings at the intersection do not form

Table 5 Extracted lengths for the outdoor near-parallelogram case (Sec. 5.4).

Trial	Line	End points	Real length (cm)	New model (cm)	Model in Ref. 9 (cm)	Model in Ref. 8 (cm)
1	L_1	IJ	79.0	83.1	65.0	103.8
2	L_2	KL	50.0	52.6	59.1	59.0
3	L_3	MN	54.5	53.9	40.2	60.7
4	L_4	OP	49.0	47.4	35.7	53.8
5	L_5	QR	75.0	71.8	60.8	60.8
6	L_6	ST	456.7	466.6	495.8	616.8
7	L_7	UV	457.8	474.2	477.2	584.8
8	L_8	SU	148.5	144.7	120.5	187.1
9	L_9	TV	153.2	151.6	102.3	154.3
10	L_{10}	WZ	214.0	219.4	248.7	221.4
11	L_{11}	A_1A_2	66.1	68.1	60.1	66.4
12	L_{12}	A_2B_1	105.5	101.3	112.4	143.3
13	L_{13}	B_2B_1	59.5	59.5	45.8	69.6
14	L_{14}	A_1B_2	131.4	128.3	146.1	174.4
15	L_{15}	C_1C_2	59.8	50.1	41.0	59.3
16	L_{16}	C_2D_1	133.7	134.7	89.1	92.9
17	L_{17}	D_2D_1	86.9	80.4	54.7	86.9
18	L_{18}	C_1D_2	132.7	138.2	123.3	131.4
19	L_{19}	E_1E_2	32.0	35.2	43.7	37.9
20	L_{20}	F_1F_2	31.5	33.1	39.6	34.7
21	L_{AB}	AB	408.1	408.5	447.9	562.6
22	L_{CD}	CD	431.6	446.3	415.2	488.5
23	L_{AC}	AC	510.0	512.5	406.0	615.8
24	L_{BD}	BD	526.1	534.2	352.3	526.8
25	L_{AD}	AD	828.0	844.2	649.6	1010.9
26	L_{CB}	CB	451.2	447.1	486.5	426.3
27	L_{EF}	EF	155.0	158.5	184.9	211.8
28	L_{GH}	GH	155.0	159.2	184.9	211.8
29	L_{EG}	EG	43.5	45.7	43.5	43.5
30	L_{FH}	FH	43.5	43.0	43.5	43.5
31	L_{EH}	EH	161.0	163.6	165.3	216.2
32	L_{GF}	GF	161.0	166.9	211.8	216.2

Table 6 Extracted lengths for the outdoor imperfect rectangle case (Sec. 5.5).

Trial	Line	End points	Real length (cm)	New model (cm)	Model in Ref. 9 (cm)	Model in Ref. 8 (cm)
1	L_1	IJ	143.5	141.0	118.4	118.5
2	L_2	KL	143.5	146.6	128.1	128.2
3	L_3	MN	143.5	139.5	134.0	134.1
4	L_4	OP	143.5	145.3	141.1	141.2
5	L_5	QR	65.5	63.6	62.4	62.4
6	L_6	ST	97.0	94.8	102.2	102.2
7	L_7	UV	87.0	84.6	90.6	90.6
8	L_8	WZ	87.0	78.1	83.6	83.6
9	L_9	A_1A_2	97.0	93.6	103.7	103.7
10	L_{10}	B_1B_2	97.0	92.8	109.5	109.5
11	L_{11}	AE	484.1	524.0	550.7	551.9
12	L_{12}	AF	711.5	729.0	773.2	775.0
13	L_{13}	AG	568.0	602.3	552.8	553.8
14	L_{14}	AH	785.1	840.0	774.9	776.4
15	L_{15}	FD	482.7	519.4	452.6	453.3
16	L_{16}	AD	1144.7	1159.6	1171.5	1174.1
17	L_{17}	GD	609.1	580.2	652.8	654.3
18	L_{18}	HD	392.5	433.0	430.3	431.2
19	L_{19}	CG	443.9	412.9	455.3	455.3
20	L_{20}	CH	385.1	352.9	451.2	451.3
21	L_{AB}	AB	770.8	793.2	891.2	892.6
22	L_{CD}	CD	628.5	647.0	764.2	765.3

Table 6 (*Continued*).

Trial	Line	End points	Real length (cm)	New model (cm)	Model in Ref. 9 (cm)	Model in Ref. 8 (cm)
23	L_{AC}	*AC*	938.1	938.1	883.9	884.6
24	L_{BD}	*BD*	939.0	914.6	807.9	808.3
25	L_{AD}	*AD*	1144.7	1159.6	1171.5	1174.1
26	L_{CB}	*CB*	1191.8	1175.3	1190.5	1190.5
27	L_{EF}	*EF*	234.4	250.2	228.8	229.3
28	L_{GH}	*GH*	223.2	241.9	228.8	229.3
29	L_{EG}	*EG*	309.7	327.9	308.8	308.8
30	L_{FH}	*FH*	307.8	328.5	308.8	308.8
31	L_{EH}	*EH*	428.1	412.7	384.4	384.6
32	L_{GF}	*GF*	334.7	324.9	384.1	384.6

a perfect rectangular shape [Fig. 19(a)], an imperfect rectangle, $ABCD$, was chosen as the calibration pattern [Fig. 19(b)]. Line AC is perpendicular to AB and CD, hence W is defined along line AC. For the control experiment, no better rectangle than $EFGH$ could be selected from the scene, so the models in Refs. 8 and 9 both used this as their calibration pattern.

Figure 19(d) shows that the estimated values (including tilt and swing angles and focal length) for the models in Refs. 8 and 9 are similar, and are different from the estimates of the new model. Again, this is probably because $EFGH$ is not a perfect rectangle, which reduces the accuracy of the models in Refs. 8 and 9. The ground truth camera height is 763.8 cm; the new model estimated the height accurately, whereas the estimates of the models in Refs. 8 and 9 were almost correct within experimental error.

Points such as the railway gauge, the lengths within the box-markings, and roadside posts were selected for accuracy evaluation. Again, the results show that the models in Refs. 8 and 9 did not perform as well as the new model; the accuracy of the former ranged from 85% to 90% with a mean of around 92%, whereas the new model did not fall below 90%, and the mean accuracy was as high as 95.6% [Fig. 19(d)]. This is entirely due to the fact that the calibration shape $EFGH$ was not a perfect rectangle, which could not be tolerated in the models in Refs. 8 and 9.

5.6 *Overall Accuracies*

The mean accuracies for each model are shown in Table 7. The models in Refs. 8 and 9 performed well in trials 1 and 2, as rectangular shapes could be found in the laboratory environment. Their performance in trial 3 was still acceptable, as it was possible to define a reasonable rectangular pattern, $EFGH$, within the box-markings. However, the performance of the models in Refs. 8 and 9 deteriorated considerably in trials 4 and 5 because only a tiny rectangle could be defined

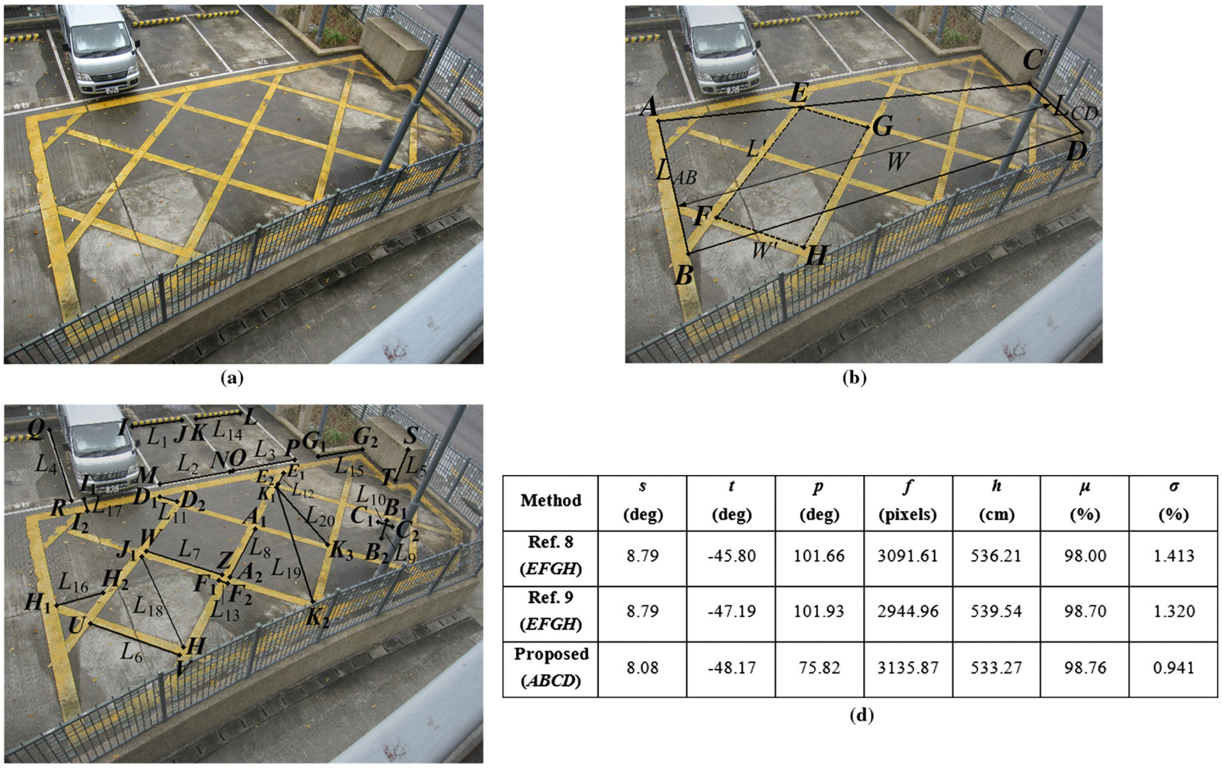
(a)

(b)

(c)

Method	*s* (deg)	*t* (deg)	*p* (deg)	*f* (pixels)	*h* (cm)	*μ* (%)	*σ* (%)
Ref. 8 (*EFGH*)	8.79	-45.80	101.66	3091.61	536.21	98.00	1.413
Ref. 9 (*EFGH*)	8.79	-47.19	101.93	2944.96	539.54	98.70	1.320
Proposed (*ABCD*)	8.08	-48.17	75.82	3135.87	533.27	98.76	0.941

(d)

Fig. 17 Outdoor trapezoidal pattern. (a) Image taken; (b) calibration pattern; (c) test lengths; and (d) computed camera parameters and percentage accuracy of length extraction.

(a) (b)

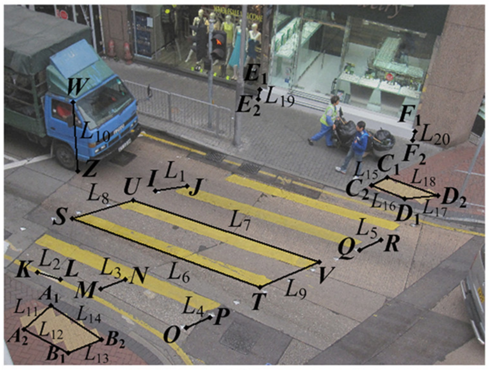

(c)

Method	s (deg)	t (deg)	p (deg)	f (pixels)	h (cm)	μ (%)	σ (%)
Ref. 8 (*EFGH*)	4.12	-47.31	18.01	3145.27	651.20	82.16	13.925
Ref. 9 (*EFGH*)	4.12	-43.08	18.63	3150.22	653.55	81.89	11.264
Proposed (*ABCD*)	4.58	-47.66	22.63	3456.50	664.63	96.60	3.178

(d)

Fig. 18 Outdoor pattern with shape close to a parallelogram. (a) Image taken; (b) calibration pattern; (c) test lengths; and (d) computed camera parameters and percentage accuracy of length extraction.

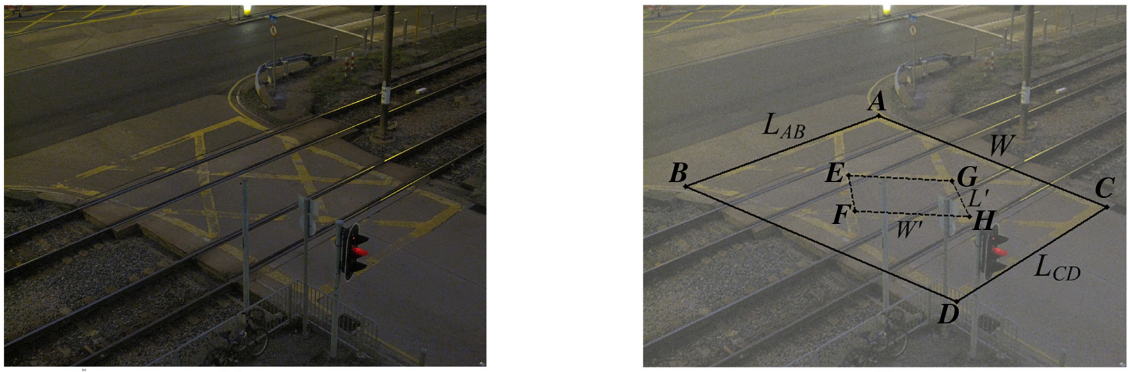

(a) (b)

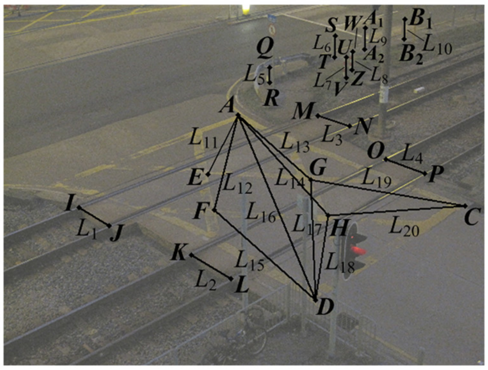

(c)

Method	s (deg)	t (deg)	p (deg)	f (pixels)	h (cm)	μ (%)	σ (%)
Ref. 8 (*EFGH*)	7.36	-44.38	89.98	7699.46	765.96	92.60	5.909
Ref. 9 (*EFGH*)	7.36	-44.45	89.95	7695.47	765.59	92.63	5.870
Proposed (*ABCD*)	7.25	-41.36	142.55	7683.20	763.23	95.55	2.848

(d)

Fig. 19 Outdoor pattern with an imperfect rectangle. (a) Image taken; (b) calibration pattern; (c) test lengths; and (d) computed camera parameters and percentage accuracy of length extraction.

Table 7 Overall accuracies.

Method	Trial 1	Trial 2	Trial 3	Trial 4	Trial 5	Average
Ref. 8	98.5%	98.2%	98.0%	82.2%	92.6%	93.9%
Ref. 9	98.5%	98.7%	98.7%	81.9%	92.6%	94.1%
Proposed	99.0%	98.6%	98.8%	96.6%	95.6%	97.7%

in trial 4, and only an imperfect rectangle could be defined in trial 5.

In contrast, the performance of the new model remained high throughout the five trials because it can accept imperfect rectangles for calibration. The average performance of the new model across the five trials was 97.7%, compared with 93.9% and 94.1% for the models in Refs. 8 and 9, respectively.

6 Conclusion

A generalized camera calibration model is proposed that eliminates the limitation of previous models, which require a perfect rectangle as a calibration pattern. The major advantage of the new model is that it can cope even in situations where there is no perfect rectangle, thus avoiding the deterioration in camera parameter estimation due to the use of imperfect or nonideal rectangular patterns. The correct computation of camera parameters is an important step in defining the 2-D/3-D transformation, which provides essential information for analyzing vehicle speeds and pedestrian flows and for estimating traffic parameters.

The proposed model was tested in both laboratory and outdoor environments, and performance was evaluated based on the length estimation of test points in 3-D. The experimental results revealed that the new model achieved an outstanding performance of 97.7%, compared with 93.9% for the model in Ref. 8 and 94.1% for the model in Ref. 9, both of which suffered from the lack of ideal rectangular patterns for calibration. The proposed method can potentially be generalized for use in a wide range of applications, such as for modeling traffic or pedestrian behavior, vehicle speed enforcement, and image metrology for forensic purposes.

Appendix: Derivation of Equations for *p*, *t*, *s*, *f* and *h*

A1 Inverse Projection when $Z_Q \neq 0$

Using the original expression from Fung's model[8] and by substituting $l = h/\sin t$, we obtain

$$X_Q = \frac{\sin p(h/\sin t + Z_Q \sin t)(x_q \sin s + y_q \cos s) + \cos p(h + Z_Q)(x_q \cos s - y_q \sin s) - Z_Q f \cos t \sin p}{x_q \cos t \sin s + y_q \cos t \cos s + f \sin t}, \tag{17}$$

and

$$Y_Q = \frac{-\cos p(h/\sin t + Z_Q \sin t)(x_q \sin s + y_q \cos s) + \sin p(h + Z_Q)(x_q \cos s - y_q \sin s) + Z_Q f \cos t \cos p}{x_q \cos t \sin s + y_q \cos t \cos s + f \sin t}. \tag{18}$$

Substitute $Z_Q = 0$, and the above equations become Eqs. (3) and (4). Equations (17) and (18) can be used to determine the 3-D coordinate of a point in the image above ground level (i.e., $Z_Q \neq 0$). The height of the point needs to be entered into the equation to estimate its X_Q and Y_Q 3-D world coordinates (i.e., $\mathbf{Q} = \Phi^{-1}\{\mathbf{q}, Z_Q\}$).[1] If the height information for that point is not available, it can be estimated by transforming two points with the same X_Q and Y_Q coordinates (but with different heights) from 2-D to 3-D using Eqs. (17) and (18). Then enter Z_Q into the equation for the upper point by trial-and-error until the X_Q and Y_Q coordinates of both points match each other in 3-D space.

A2 Proof of Case I: Trapezoidal Case ($L_{AB} \neq L_{CD}$)

First, let the four corners A, B, C and D of the calibration pattern, defined by the lane markings in the image, be $a(x_a, y_a)$, $b(x_b, y_b)$, $c(x_c, y_c)$ and $d(x_d, y_d)$, respectively. To simplify the inverse projection equations (Φ^{-1}), let $\Lambda_Q = x_q \sin s + y_q \cos s$, and $\Gamma_Q = x_q \cos s - y_q \sin s$, and substitute into Eqs. (3) and (4):

$$X_Q = \frac{h \sin p \cdot \Lambda_Q / \sin t + h \cos p \cdot \Gamma_Q}{\cos t \cdot \Lambda_Q + f \sin t} = \frac{h \cos p}{\sin t \cos t} \cdot \left(\frac{\Lambda_Q \tan p + \Gamma_Q \sin t}{\Lambda_Q + f \tan t}\right),$$

and

$$Y_Q = \frac{-h \cos p \cdot \Lambda_Q / \sin t + h \sin p \cdot \Gamma_Q}{\cos t \cdot \Lambda_Q + f \sin t} = \frac{h \cos p}{\sin t \cos t} \cdot \left(\frac{\Gamma_Q \tan p \sin t - \Lambda_Q}{\Lambda_Q + f \tan t}\right).$$

Further, let $\varphi = f \tan t$, then

$$X_Q = \frac{h \cos p}{\sin t \cos t} \cdot \left(\frac{\Lambda_Q \tan p + \Gamma_Q \sin t}{\Lambda_Q + \varphi}\right), \tag{19}$$

and

$$Y_Q = \frac{h \cos p}{\sin t \cos t} \cdot \left(\frac{\Gamma_Q \tan p \sin t - \Lambda_Q}{\Lambda_Q + \varphi}\right). \tag{20}$$

A2.1 *Equating Conditions 1 and 2 to Form an Expression for p and φ*

Equate condition 1 (i.e., $Y_A = Y_B$) by expressing it in terms of Eq. (20) for Y_A and Y_B:

$$\frac{\Gamma_A \tan p \sin t - \Lambda_A}{\Lambda_A + \varphi} = \frac{\Gamma_B \tan p \sin t - \Lambda_B}{\Lambda_B + \varphi}.$$

Therefore,

$$\tan p = \frac{1}{\sin t} \cdot \left[\frac{(\Lambda_A - \Lambda_B)\varphi}{\Gamma_A\Lambda_B - \Gamma_B\Lambda_A + (\Gamma_A - \Gamma_B)\varphi}\right]. \tag{21}$$

Equate condition 2 (i.e., $Y_C = Y_D$) in the same manner:

$$\tan p = \frac{1}{\sin t} \cdot \left[\frac{(\Lambda_C - \Lambda_D)\varphi}{\Gamma_C\Lambda_D - \Gamma_D\Lambda_C + (\Gamma_C - \Gamma_D)\varphi}\right]. \tag{22}$$

Combine Eqs. (21) and (22) to find an expression for φ:

$$\frac{(\Lambda_A - \Lambda_B)\varphi}{\Gamma_A\Lambda_B - \Gamma_B\Lambda_A + (\Gamma_A - \Gamma_B)\varphi} = \frac{(\Lambda_C - \Lambda_D)\varphi}{\Gamma_C\Lambda_D - \Gamma_D\Lambda_C + (\Gamma_C - \Gamma_D)\varphi}$$

Therefore,

$$\varphi = -\frac{(\Gamma_A\Lambda_B - \Gamma_B\Lambda_A)(\Lambda_C - \Lambda_D) - (\Gamma_C\Lambda_D - \Gamma_D\Lambda_C)(\Lambda_A - \Lambda_B)}{(\Gamma_A - \Gamma_B)(\Lambda_C - \Lambda_D) - (\Gamma_C - \Gamma_D)(\Lambda_A - \Lambda_B)}. \tag{23}$$

A2.2 *Equating Conditions 3 and 5 to Form an Expression for p*

Apply Eq. (19) to condition 3: $X_B - X_A = L_{AB}$,

$$\frac{\Lambda_B \tan p + \Gamma_B \sin t}{\Lambda_B + \varphi} - \frac{\Lambda_A \tan p + \Gamma_A \sin t}{\Lambda_A + \varphi} = \frac{L_{AB} \sin t \cos t}{h \cos p}. \tag{24}$$

Apply Eq. (20) to condition 5: $Y_C - Y_A = W$,

$$\frac{\Gamma_C \tan p \sin t - \Lambda_C}{\Lambda_C + \varphi} - \frac{\Gamma_A \tan p \sin t - \Lambda_A}{\Lambda_A + \varphi} = \frac{W \sin t \cos t}{h \cos p}. \tag{25}$$

Divide Eq. (24) by Eq. (25):

$$\frac{\Lambda_B \tan p + \Gamma_B \sin t}{\Lambda_B + \varphi} - \frac{\Lambda_A \tan p + \Gamma_A \sin t}{\Lambda_A + \varphi} = \frac{L_{AB}}{W}\left(\frac{\Gamma_C \tan p \sin t - \Lambda_C}{\Lambda_C + \varphi} - \frac{\Gamma_A \tan p \sin t - \Lambda_A}{\Lambda_A + \varphi}\right).$$

To solve p:

$$\tan p = \frac{\left\{\begin{array}{l} \frac{L_{AB}}{W}[\Lambda_A(\Lambda_B + \varphi)(\Lambda_C + \varphi) - \Lambda_C(\Lambda_A + \varphi)(\Lambda_B + \varphi)] \\ +[\Gamma_A(\Lambda_B + \varphi)(\Lambda_C + \varphi) - \Gamma_B(\Lambda_A + \varphi)(\Lambda_C + \varphi)] \sin t \end{array}\right\}}{\left\{\begin{array}{l} [\Lambda_B(\Lambda_A + \varphi)(\Lambda_C + \varphi) - \Lambda_A(\Lambda_B + \varphi)(\Lambda_C + \varphi)] \\ + \frac{L_{AB}}{W}[\Gamma_A(\Lambda_B + \varphi)(\Lambda_C + \varphi) - \Gamma_C(\Lambda_A + \varphi)(\Lambda_B + \varphi)] \sin t \end{array}\right\}}. \tag{26}$$

A2.3 *Combine p from A2.1 and A2.2 to Derive an Expression for t*

Combining Eqs. (21) and (26):

$$\frac{1}{\sin t} \cdot \left[\frac{(\Lambda_A - \Lambda_B)\varphi}{\Gamma_A\Lambda_B - \Gamma_B\Lambda_A + (\Gamma_A - \Gamma_B)\varphi}\right] = \frac{\left\{\begin{array}{l} \frac{L_{AB}}{W}[\Lambda_A(\Lambda_B + \varphi)(\Lambda_C + \varphi) - \Lambda_C(\Lambda_A + \varphi)(\Lambda_B + \varphi)] \\ +[\Gamma_A(\Lambda_B + \varphi)(\Lambda_C + \varphi) - \Gamma_B(\Lambda_A + \varphi)(\Lambda_C + \varphi)] \sin t \end{array}\right\}}{\left\{\begin{array}{l} [\Lambda_B(\Lambda_A + \varphi)(\Lambda_C + \varphi) - \Lambda_A(\Lambda_B + \varphi)(\Lambda_C + \varphi)] \\ + \frac{L_{AB}}{W}[\Gamma_A(\Lambda_B + \varphi)(\Lambda_C + \varphi) - \Gamma_C(\Lambda_A + \varphi)(\Lambda_B + \varphi)] \sin t \end{array}\right\}}.$$

Expanding it produces the following quadratic form:

$$\begin{aligned} &\sin^2 t[\Gamma_A(\Lambda_B + \varphi)(\Lambda_C + \varphi) - \Gamma_B(\Lambda_A + \varphi)(\Lambda_C + \varphi)] \\ &\quad + \sin t \frac{L_{AB}}{W}\left\{\begin{array}{l} [\Lambda_A(\Lambda_B + \varphi)(\Lambda_C + \varphi) - \Lambda_C(\Lambda_A + \varphi)(\Lambda_B + \varphi)] \\ -[\Gamma_A(\Lambda_B + \varphi)(\Lambda_C + \varphi) - \Gamma_C(\Lambda_A + \varphi)(\Lambda_B + \varphi)]\left[\frac{(\Lambda_A - \Lambda_B)\varphi}{\Gamma_A\Lambda_B - \Gamma_B\Lambda_A + (\Gamma_A - \Gamma_B)\varphi}\right] \end{array}\right\} \\ &\quad + [\Lambda_A(\Lambda_B + \varphi)(\Lambda_C + \varphi) - \Lambda_B(\Lambda_A + \varphi)(\Lambda_C + \varphi)]\left[\frac{(\Lambda_A - \Lambda_B)\varphi}{\Gamma_A\Lambda_B - \Gamma_B\Lambda_A + (\Gamma_A - \Gamma_B)\varphi}\right] = 0. \end{aligned} \tag{27}$$

Let $\nu_{AB} = \frac{(\Lambda_A - \Lambda_B)\varphi}{\Gamma_A\Lambda_B - \Gamma_B\Lambda_A + (\Gamma_A - \Gamma_B)\varphi}$,

$$\begin{aligned}\alpha_{\langle e\rangle\langle f\rangle\langle g\rangle,\langle h\rangle\langle i\rangle\langle j\rangle} &= \Gamma_{\langle e\rangle}(\Lambda_{\langle f\rangle} + \varphi)(\Lambda_{\langle g\rangle} + \varphi) \\ &\quad - \Gamma_{\langle h\rangle}(\Lambda_{\langle i\rangle} + \varphi)(\Lambda_{\langle j\rangle} + \varphi),\end{aligned}$$

and

$$\begin{aligned}\beta_{\langle e\rangle\langle f\rangle\langle g\rangle,\langle h\rangle\langle i\rangle\langle j\rangle} &= \Lambda_{\langle e\rangle}(\Lambda_{\langle f\rangle} + \varphi)(\Lambda_{\langle g\rangle} + \varphi) \\ &\quad - \Lambda_{\langle h\rangle}(\Lambda_{\langle i\rangle} + \varphi)(\Lambda_{\langle j\rangle} + \varphi),\end{aligned}$$

e.g.,

$$\alpha_{ABC,BAC} = \Gamma_A(\Lambda_B + \varphi)(\Lambda_C + \varphi) - \Gamma_B(\Lambda_A + \varphi)(\Lambda_C + \varphi),$$

and

$$\beta_{ABC,CAB} = \Lambda_A(\Lambda_B + \varphi)(\Lambda_C + \varphi) - \Lambda_C(\Lambda_A + \varphi)(\Lambda_B + \varphi).$$

Applying these expressions in Eq. (27) gives

$$\alpha_{ABC,BAC} \sin^2 t + \frac{L_{AB}}{W}(\beta_{ABC,CAB} - \nu_{AB} \cdot \alpha_{ABC,CAB}) \sin t + \nu_{AB} \cdot \beta_{ABC,BAC} = 0.$$

Therefore,

$$\sin^2 t + \frac{L_{AB}}{W} \cdot \frac{\beta_{ABC,CAB} - \nu_{AB} \cdot \alpha_{ABC,CAB}}{\alpha_{ABC,BAC}} \sin t + \frac{\nu_{AB} \cdot \beta_{ABC,BAC}}{\alpha_{ABC,BAC}} = 0. \tag{28}$$

Further, let $\kappa_1 = \frac{L_{AB}}{W} \cdot \frac{\beta_{ABC,CAB} - \nu_{AB} \cdot \alpha_{ABC,CAB}}{\alpha_{ABC,BAC}}$ and $\kappa_2 = \frac{\nu_{AB} \cdot \beta_{ABC,BAC}}{\alpha_{ABC,BAC}}$, then Eq. (28) becomes

$$\sin^2 t + \kappa_1 \sin t + \kappa_2 = 0. \tag{29}$$

Solving for sin t, we have:

$$\sin\ t = \frac{-\kappa_1 \pm \sqrt{\kappa_1^2 - 4\kappa_2}}{2}. \tag{30}$$

A2.4 *Equating Conditions 4 and 5 to Form Another Expression for t*

From conditions 4 and 5 (i.e., $X_D - X_C = L_{CD}$ and $Y_C - Y_A = W$), we can obtain the following according to the steps in Secs. A2.2 and A2.3:

$$\sin\ t = \frac{-\kappa_3 \pm \sqrt{\kappa_3^2 - 4\kappa_4}}{2}, \tag{31}$$

where $\kappa_3 = \frac{L_{CD}}{W} \cdot \frac{\beta_{ADC,CAD} - \nu_{AB} \cdot \alpha_{ADC,CAD}}{\alpha_{CDA,DAC}}$ and $\kappa_4 = \frac{\nu_{AB} \cdot \beta_{CDA,DAC}}{\alpha_{CDA,DAC}}$.

A2.5 *Combining Both Expressions of t to Form a Numerical Solution for s*

Combining Eqs. (30) and (31) gives:

$$-\kappa_1 + \sqrt{\kappa_1^2 - 4\kappa_2} = -\kappa_3 + \sqrt{\kappa_3^2 - 4\kappa_4}. \tag{32}$$

Therefore, solving the swing angle (s) is equivalent to the following minimization problem:

$$\arg\min_s |(-\kappa_1 + \kappa_3) + (\sqrt{\kappa_1^2 - 4\kappa_2} - \sqrt{\kappa_3^2 - 4\kappa_4})|, \tag{33}$$

which becomes Eq. (10).

A2.6 *Equations for the Remaining Camera Parameters*

From Eq. (30), the tilt angle (t) can be computed as

$$t = \sin^{-1}\left(\frac{-\kappa_1 \pm \sqrt{\kappa_1^2 - 4\kappa_2}}{2}\right), \tag{34}$$

which becomes Eq. (11).

Using Eq. (21) to calculate the pan angle (p):

$$p = \tan^{-1}\left\{\frac{1}{\sin\ t} \cdot \left[\frac{(\Lambda_A - \Lambda_B)\varphi}{\Gamma_A\Lambda_B - \Gamma_B\Lambda_A + (\Gamma_A - \Gamma_B)\varphi}\right]\right\}.$$

Substituting the expression ν_{AB} as defined in Sec. A2.3, the equation becomes:

$$p = \tan^{-1}(\nu_{AB}/\sin\ t) \tag{35}$$

which becomes Eq. (12).

The focal length (f) can be calculated from the original definition of φ at the beginning of Sec. A2, which forms Eq. (13):

$$f = \varphi/\tan\ t. \tag{36}$$

Using Eq. (25) to compute h becomes Eq. (14):

$$h = \frac{W \sin t \cos t}{\cos p} \times \left(\frac{\Gamma_C \tan p \sin t - \Lambda_C}{\Lambda_C + \varphi} - \frac{\Gamma_A \tan p \sin t - \Lambda_A}{\Lambda_A + \varphi}\right)^{-1}. \tag{37}$$

This forms a complete derivation for the set of equations in Sec. 4.2.3 when $L_{AB} \neq L_{CD}$.

A3 Proof of Case II: Parallelogram Case ($L_{AB} = L_{CD}$ and $\varepsilon_{AC} = \varepsilon_{BD} \neq 0$)

A3.1 *Manipulating Conditions 3 and 4 in Terms of ε*

When $L_{AB} = L_{CD} = L$, Conditions 3 and 4 become $X_B - X_A = X_D - X_C = L$. Rearranging the terms, it becomes $X_C - X_A = X_D - X_B$.

Let

$$X_C - X_A = X_D - X_B = \varepsilon, \tag{38}$$

where ε is a constant, which corresponds to Fig. 4(a) in Sec. 2.

A3.2 *Combining Eq. (38) and Condition 5 to Form an Expression for p*

Apply Eq. (19) to Eq. (38): $X_C - X_A = \varepsilon$,

$$\frac{\Lambda_C\ \tan\ p + \Gamma_C\ \sin\ t}{\Lambda_C + \varphi} - \frac{\Lambda_A\ \tan\ p + \Gamma_A\ \sin\ t}{\Lambda_A + \varphi} = \frac{\varepsilon\ \sin\ t\ \cos\ t}{h\ \cos\ p}. \tag{39}$$

Divide Eq. (39) by Eq. (25) in Sec. A2.2,

$$\begin{aligned}(\Lambda_C \tan p + \Gamma_C \sin t)(\Lambda_A + \varphi)\\ - (\Lambda_A \tan p + \Gamma_A \sin t)(\Lambda_C + \varphi)\\ = \frac{\varepsilon}{W}[(\Gamma_C \sin t \tan p - \Lambda_C)(\Lambda_A + \varphi)\\ - (\Gamma_A \sin t \tan p - \Lambda_A)(\Lambda_C + \varphi)].\end{aligned} \tag{40}$$

Isolating $\tan p$ gives the following equation:

$$\tan p = \frac{\frac{\varepsilon}{W}(\Lambda_C - \Lambda_A)\varphi + [\Gamma_C\Lambda_A - \Gamma_A\Lambda_C + (\Gamma_C - \Gamma_A)\varphi] \sin t}{(\Lambda_A - \Lambda_C)\varphi + \frac{\varepsilon}{W}[\Gamma_C\Lambda_A - \Gamma_A\Lambda_C + (\Gamma_C - \Gamma_A)\varphi] \sin t}. \tag{41}$$

A3.3 *Combining Eq. (38) and Another Compatible Version of Condition 5*

Apply Eq. (19) to the other term of Eq. (38): $X_D - X_B = \varepsilon$,

$$\frac{\Lambda_D \tan p + \Gamma_D \sin t}{\Lambda_D + \varphi} - \frac{\Lambda_B \tan p + \Gamma_B \sin t}{\Lambda_B + \varphi} = \frac{\varepsilon \sin t \cos t}{h \cos p}. \tag{42}$$

Another compatible version of condition 5 is $Y_D - Y_B = W$. Applying Eq. (20) to this condition gives

$$\frac{\Gamma_D \tan p \sin t - \Lambda_D}{\Lambda_D + \varphi} - \frac{\Gamma_B \tan p \sin t - \Lambda_B}{\Lambda_B + \varphi} = \frac{W \sin t \cos t}{h \cos p}. \tag{43}$$

Similarly, divide Eq. (42) by (43), then isolate $\tan p$ to obtain

$$\tan p = \frac{\frac{\varepsilon}{W}(\Lambda_D - \Lambda_B)\varphi + [\Gamma_D\Lambda_B - \Gamma_B\Lambda_D + (\Gamma_D - \Gamma_B)\varphi] \sin t}{(\Lambda_B - \Lambda_D)\varphi + \frac{\varepsilon}{W}[\Gamma_D\Lambda_B - \Gamma_B\Lambda_D + (\Gamma_D - \Gamma_B)\varphi] \sin t}. \tag{44}$$

A3.4 *Combine p from A3.2 and A3.3 to Solve for φ*

Combine Eqs. (41) and (44), and isolating φ gives

$$\varphi = -\frac{(\Gamma_C\Lambda_A - \Gamma_A\Lambda_C)(\Lambda_D - \Lambda_B) - (\Gamma_D\Lambda_B - \Gamma_B\Lambda_D)(\Lambda_C - \Lambda_A)}{(\Gamma_C - \Gamma_A)(\Lambda_D - \Lambda_B) - (\Gamma_D - \Gamma_B)(\Lambda_C - \Lambda_A)}. \tag{45}$$

A3.5 *Combine Both Expressions of φ to Solve for s*

Equating Eqs. (23) and (45), we have

$$\begin{aligned}&\frac{(\Gamma_A\Lambda_B - \Gamma_B\Lambda_A)(\Lambda_C - \Lambda_D) - (\Gamma_C\Lambda_D - \Gamma_D\Lambda_C)(\Lambda_A - \Lambda_B)}{(\Gamma_A - \Gamma_B)(\Lambda_C - \Lambda_D) - (\Gamma_C - \Gamma_D)(\Lambda_A - \Lambda_B)}\\ &= \frac{(\Gamma_C\Lambda_A - \Gamma_A\Lambda_C)(\Lambda_D - \Lambda_B) - (\Gamma_D\Lambda_B - \Gamma_B\Lambda_D)(\Lambda_C - \Lambda_A)}{(\Gamma_C - \Gamma_A)(\Lambda_D - \Lambda_B) - (\Gamma_D - \Gamma_B)(\Lambda_C - \Lambda_A)}.\end{aligned} \tag{46}$$

Let $\chi_{PQ} = x_q - x_p$, $\gamma_{PQ} = y_q - y_p$, and $\zeta_{PQ} = x_p y_q - x_q y_p$, then $\Lambda_P - \Lambda_Q = -\chi_{PQ} \sin s - \gamma_{PQ} \cos s$, $\Gamma_P - \Gamma_Q = -\chi_{PQ} \cos s + \gamma_{PQ} \sin s$, and $\Gamma_P\Lambda_Q - \Gamma_Q\Lambda_P = \zeta_{PQ}$. Equation (46) then becomes

$$\begin{aligned}&\frac{\zeta_{AB}(-\chi_{CD} \sin s - \gamma_{CD} \cos s) - \zeta_{CD}(-\chi_{AB} \sin s - \gamma_{AB} \cos s)}{\left[\begin{array}{l}(-\chi_{AB} \cos s + \gamma_{AB} \sin s)(-\chi_{CD} \sin s - \gamma_{CD} \cos s)\\ -(-\chi_{CD} \cos s + \gamma_{CD} \sin s)(-\chi_{AB} \sin s - \gamma_{AB} \cos s)\end{array}\right]}\\ &= \frac{\zeta_{AC}(-\chi_{BD} \sin s - \gamma_{BD} \cos s) - \zeta_{BD}(-\chi_{AC} \sin s - \gamma_{AC} \cos s)}{\left[\begin{array}{l}(-\chi_{AC} \cos s + \gamma_{AC} \sin s)(-\chi_{BD} \sin s - \gamma_{BD} \cos s)\\ -(-\chi_{BD} \cos s + \gamma_{BD} \sin s)(-\chi_{AC} \sin s - \gamma_{AC} \cos s)\end{array}\right]}.\end{aligned} \tag{47}$$

By isolating s in Eq. (47), the closed-form solution of s [i.e., Eq. (15)] can be derived.

A4 Reduction of Model Case III: Rectangular Case ($L_{AB} = L_{CD}$ and $\varepsilon_{AC} = \varepsilon_{BD} = 0$)

Combine Eqs. (21) and (41):

$$\begin{aligned}&\frac{1}{\sin t}\left[\frac{(\Lambda_A - \Lambda_B)\varphi}{\Gamma_A\Lambda_B - \Gamma_B\Lambda_A + (\Gamma_A - \Gamma_B)\varphi}\right]\\ &= \frac{\frac{\varepsilon}{W}(\Lambda_C - \Lambda_A)\varphi + [\Gamma_C\Lambda_A - \Gamma_A\Lambda_C + (\Gamma_C - \Gamma_A)\varphi] \sin t}{(\Lambda_A - \Lambda_C)\varphi + \frac{\varepsilon}{W}[\Gamma_C\Lambda_A - \Gamma_A\Lambda_C + (\Gamma_C - \Gamma_A)\varphi] \sin t}.\end{aligned} \tag{48}$$

Cross multiplying both sides and reorganizing the fraction gives the quadratic equation

$$\begin{aligned}\sin^2 t + \frac{\varepsilon}{W}&\left[\frac{(\Lambda_A - \Lambda_C)\varphi}{\Gamma_A\Lambda_C - \Gamma_C\Lambda_A + (\Gamma_A - \Gamma_C)\varphi}\right.\\ &\left. - \frac{(\Lambda_A - \Lambda_B)\varphi}{\Gamma_A\Lambda_B - \Gamma_B\Lambda_A + (\Gamma_A - \Gamma_B)\varphi}\right] \sin t\\ &+ \left[\frac{(\Lambda_A - \Lambda_C)\varphi}{\Gamma_A\Lambda_C - \Gamma_C\Lambda_A + (\Gamma_A - \Gamma_C)\varphi}\right]\\ &\times \left[\frac{(\Lambda_A - \Lambda_B)\varphi}{\Gamma_A\Lambda_B - \Gamma_B\Lambda_A + (\Gamma_A - \Gamma_B)\varphi}\right] = 0.\end{aligned} \tag{49}$$

To simplify the quadratic form, let $\nu_{PQ} = \frac{(\Lambda_P - \Lambda_Q)\varphi}{\Gamma_P\Lambda_Q - \Gamma_Q\Lambda_P + (\Gamma_P - \Gamma_Q)\varphi}$ and substitute into the equation, so that

$$\sin^2 t + \frac{\varepsilon}{W}(\nu_{AC} - \nu_{AB}) \sin t + \nu_{AC}\nu_{AB} = 0. \tag{50}$$

Solving the quadratic equation, we have

$$\begin{aligned}\sin t = &-\frac{\varepsilon}{2W}(\nu_{AC} - \nu_{AB})\\ &\pm \frac{1}{2}\sqrt{\left[\frac{\varepsilon}{W}(\nu_{AC} - \nu_{AB})\right]^2 - 4\nu_{AC}\nu_{AB}}.\end{aligned} \tag{51}$$

When $\varepsilon = 0$, Eq. (51) becomes

$$t = \sin^{-1}\left(-\frac{1}{2}\sqrt{-4\nu_{AC}\nu_{AB}}\right) = \sin^{-1}\left(-\sqrt{-\nu_{AC}\nu_{AB}}\right), \tag{52}$$

which is essentially Eq. (16).

A5 Details of the Extracted Lengths

The extracted lengths are depicted in Tables 2 to 6.

Acknowledgments

The work described in this paper was jointly supported by grants from the Research Grants Council of the Hong Kong Special Administrative Region, China (No. HKU7184/10E), the Engineering Postdoctoral Fellowship Programme of the University of Hong Kong, and the National Research Foundation of Korea grant funded by the Korean government (MEST) (No. NRF-2010-0029446).

References

1. A. H. S. Lai, G. S. K. Fung, and N. H. C. Yung, “Vehicle type classification from visual-based dimension estimation,” in *Proc. IEEE Conference on Intelligent Transportation Systems*, pp. 201–206, IEEE, Oakland, CA (2001).
2. G. S. K. Fung, N. H. C. Yung, and G. K. H. Pang, “Vehicle shape approximation from motion for visual traffic surveillance,” in *Proc. IEEE Conference on Intelligent Transportation Systems*, pp. 608–613, IEEE, Oakland, CA (2001).
3. M. Sonka, V. Hlavac, and R. Boyle, *Image Processing, Analysis and Machine Vision*, Chapter 11, Thompson Learning, Toronto (2008).
4. J. C. T. Diaz et al., “A camera auto-calibration algorithm for realtime road traffic analysis,” in *Comput. Vision Theory Appl.*, Lisboa, Portugal, pp. 626–631 (2009).
5. J. Heikkila, “Geometric camera calibration using circular control points,” *IEEE Trans. Pattern Anal. Mach. Intell.* **22**(10), 1066–1077 (2000).
6. A. Datta, J. S. Kim, and T. Kanade, “Accurate camera calibration using iterative refinement of control points,” in *Proc. IEEE Int. Conf. Comput. Vision*, pp. 1201–1208, IEEE, Kyoto (2009).
7. J. W. Courtney, M. J. Magee, and J. K. Aggarwal, “Robot guidance using computer vision,” *Pattern Recognit.* **17**(6), 585–592 (1984).
8. G. S. K. Fung, N. H. C. Yung, and G. K. H. Pang, “Camera calibration from road lane markings,” *Opt. Eng.* **42**(10), 2967–2977 (2003).
9. X. C. He and N. H. C. Yung, “New method for overcoming ill-conditioning in vanishing-point-based camera calibration,” *Opt. Eng.* **46**(3), 037202 (2007).
10. A. Gruen and T. S. Huang, *Calibration and Orientation of Cameras in Computer Vision*, Springer-Verlag, Berlin (2010).
11. A. K. Chong, “A rigorous technique for forensic measurement of surveillance video footage,” *Photogramm. Eng. Remote Sens.* **68**(7), 753–759 (2002).
12. I. Fukui, “TV image processing to determine the position of a robot vehicle,” *Pattern Recognit.* **14**(1–6), 101–109 (1981).
13. W. H. Chou and W. H. Tsai, “A new approach to robot location by house corners,” *Pattern Recognit.* **19**(6), 439–451 (1986).
14. R. Y. Tsai, “A versatile camera calibration technique for high-accuracy 3D machine vision metrology using off-the-shelf TV cameras and lenses,” *IEEE J. Robot. Autom.* **3**(4), 323–344 (1987).
15. L. L. Wang and W. H. Tsai, “Camera calibration by vanishing lines for 3-D computer vision,” *IEEE Trans. Pattern Anal. Mach. Intell.* **13**(4), 370–376 (1991).
16. E. K. Bas and J. D. Crisman, “An easy to install camera calibration for traffic monitoring,” in *Proc. IEEE Conference on Intelligent Transportation Systems*, pp. 362–366, IEEE, Boston, MA (1997).
17. T. N. Schoepflin and D. J. Dailey, “Dynamic camera calibration of roadside traffic management cameras for vehicle speed estimation,” *IEEE Trans. Intell. Transp. Syst.* **4**(2), 90–98 (2003).
18. A. H. S. Lai, “An Effective Methodology for Visual Traffic Surveillance,” Ph.D. Thesis, The University of Hong Kong (2000).
19. M. Haralick, “Using perspective transformations in scene analysis,” *Comput. Graph. Image Process.* **13**(3), 191–221 (1980).

Clement Chun Cheong Pang received BEng and MEng degrees in electrical and computer engineering from McMaster University, Hamilton, Ontario, Canada, in 1999 and 2001, respectively, and a PhD degree in electrical and electronic engineering from the University of Hong Kong (HKU), Hong Kong, in 2005. After graduation, he joined the Hong Kong Police Force to work as a Research Scientist for the Technical Services Division, Crime Wing, to develop automation applications for frontline police officers. After that, he joined HKU again to work as a post-doctoral fellow in the Transportation Laboratory of Department of Civil Engineering, in 2011. His research interests include intelligent transportation systems, crowd behavior modeling, and railway asset management. He is a member of SPIE.

Seakay Siqi Xie received her BEng degree in civil engineering and MPhil degree in transportation engineering from the University of Hong Kong (HKU), Hong Kong. She is currently working toward a PhD degree with the Transportation Laboratory, Department of Civil Engineering, HKU. Her research interests include pedestrian flow modeling and pedestrian safety.

Sze Chun Wong received his BSc (Eng) and MPhil degrees from the University of Hong Kong (HKU), and PhD degree from University College London. He is currently a chair professor with the Department of Civil Engineering of HKU. His research interests include optimization of traffic signal settings, continuum modeling for traffic equilibrium problems, land use and transportation problems, dynamic highway and transit assignment problems, urban taxi services, and road safety.

Keechoo Choi is a professor of transportation engineering and associate dean of the graduate school of ITS at Ajou University. He is the managing editor of *International Journal of Sustainable Transportation* (SSCI), editorial board member of Journal of ITS, Transportmetrica Part B, and serves for various international journal review members. He is the director of the TOD-based Sustainable City/Transportation Research Engineering Center funded by the Korean government of Ministry of Education, Science and Technology. He represents the technical committee of 2.2 of the Korean national board of World Road Association, PIARC. He eagerly attends TRB, WCTR, and ITS WC as a researcher. His specialties include travel demand forecasting, travel time estimation for ITS, sustainable transportation with environmental concerns, and public transportation issues.